Table 1 Baseline characteristics

Characteristics	Candesartan (n = 158)	Amlodipine (n = 160)	P-value
Age (years)	66.0 ± 9.7	65.1 ± 9.3	0.429
Male (%)	109 (69.0)	110 (68.8)	0.905
SBP (mmHg)	139.5 ± 15.4	140.7 ± 15.5	0.486
DBP (mmHg)	81.0 ± 11.3	82.5 ± 11.2	0.256
Heart rate (bpm)	70.9 ± 14.4	69.5 ± 13.9	0.379
Duration of AF			0.818
<1 year	41 (25.9)	37 (23.1)	
≤1, <5 years	57 (36.1)	66 (41.3)	
>5 years	43 (27.2)	41 (25.6)	
Unknown	17 (10.8)	16 (10)	
Coexisting conditions			
Prior embolism (%)	12 (7.6)	12 (7.5)	1.000
Heart failure (%)	4 (2.5)	4 (2.5)	1.000
Myocardial infarction (%)	3 (1.9)	1 (0.6)	0.370
Angina pectoris (%)	3 (1.9)	4 (2.5)	1.000
Cardiomyopathy (%)	4 (2.5)	3 (1.9)	0.690
Valvular disease (%)	9 (5.7)	14 (8.8)	0.387
Diabetes (%)	15 (9.5)	14 (8.8)	0.848
Hyperlipidaemia (%)	47 (29.7)	47 (29.4)	1.000
Echocardiograms			
LVDd	47.5 ± 4.9	47.87 ± 4.9	0.549
LVEF	69.1 ± 8.1	66.2 ± 8.2	0.003
LAD	38.9 ± 6.7	39.3 ± 6.8	0.618
Treatment at baseline			
Anti-hypertensive therapy (%)	120 (75.9)	124 (77.5)	0.791
AAD (%)	105 (66.5)	119 (74.4)	0.141
PAF frequency during observation period			
Total PAF (days/month)	3.8 ± 5.0	4.8 ± 6.3	0.116
Symptomatic PAF	1.4 ± 3.0	1.4 ± 2.9	0.903
Treatment at initial follow-up			
Candesartan	8.0 ± 2.7 mg/day	—	—
Amlodipine	—	4.3 ± 1.7 mg/day	—
Diuretics (%)	20 (12.7)	9 (5.6)	0.029
β-Blockers (%)	48 (30.4)	50 (31.3)	0.867
Antiplatelet therapy (%)	46 (29.1)	48 (30.0)	0.863
Anticoagulant therapy (%)	80 (50.6)	88 (55.0)	0.435
Statins (%)	26 (16.5)	24 (15.0)	0.721

Data represent mean ± SD or frequency. SBP, systolic blood pressure; DBP, diastolic blood pressure; PAF, paroxysmal atrial fibrillation; LVDd, left ventricular diastolic diameter; LVEF, left ventricular ejection fraction; LAD, left atrial dimension; AAD, antiarrhythmic drug; bpm, beat per minute. Anti-hypertensive therapy includes ACE-inhibitors, angiotensin receptor blockers, calcium channel blockers, β-blockers, α-blockers, and diuretics.

n = 95), and a higher group (≥139 mmHg, n = 105). There were no significant differences between the two groups in the reduction in AF frequency during the follow-up period in any subset analysis (Table 3).

Discussion

In the present J-RHYTHM II study, we tested a hypothesis that, in patients with paroxysmal AF associated with hypertension, candesartan may exert beneficial effect on the frequency of paroxysmal AF when compared with conventional hypertension therapy with

amlodipine. In our study population, we could not find any differences between the two therapies in the nature of paroxysmal AF during the maximal follow-up of 1 year. These results were essentially unaffected by subgroup analyses depending on the systolic BP attained by the therapies. Our findings, in concordance with a recent GISSI-AF study,[13] do not support the concept that the blockade of RAS may have a favourable effect on the occurrence of AF beyond the control of BP.

There is considerable experimental evidence suggesting that the administration of angiotensin II-receptor blockers (ARB) may prevent or reverse the progression of atrial fibrosis in association
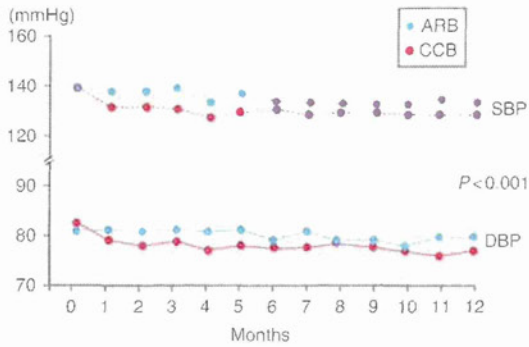
Figure 1 The time-course of systolic blood pressure and diastolic blood pressure in the candesartan (angiotensin II-receptor blocker) and amlodipine (calcium channel blocker) group. There were significant differences both in systolic and diastolic blood pressure between the groups ($P < 0.0001$ by ANOVA).
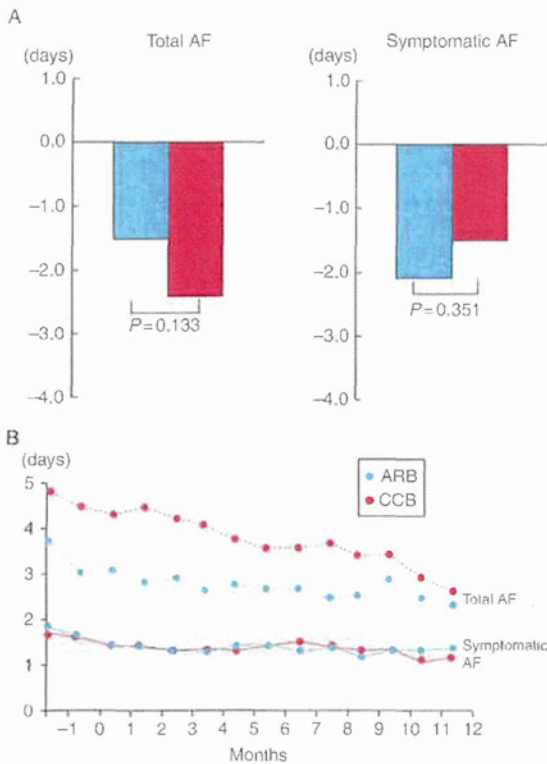
Table 2 Secondary endpoints

	Candesartan ($n = 158$)	Amlodipine ($n = 160$)	P-value
Cardiovascular events (%)			
Cardiovascular death	0 (0.0)	0 (0.0)	—
Acute myocardial infarction	0 (0.0)	0 (0.0)	—
Stroke	0 (0.0)	3 (1.8)	0.084
Major bleeding	0 (0.0)	1 (0.6)	0.320
Heart failure	0 (0.0)	0 (0.0)	—
Development of persistent AF	13 (8.2)	24 (15.0)	0.080
Changes in LAD	+0.34 ± 5.8	+0.25 ± 4.9	0.895
Changes in QOL assessment			
AFQLQ1	+0.9 ± 5.6	+1.8 ± 6.0	0.246
AFQLQ2	+1.5 ± 3.8	+2.2 ± 4.2	0.189
AFQLQ3	+1.6 ± 7.4	+2.6 ± 10.0	0.412

Data represent mean ± SD or frequency. AFQLQ1, frequency of symptoms; AFQLQ2, severity of symptoms; AFQLQ3, limitations of daily activities and mental anxiety (higher is better in these components).

Table 3 Frequency of paroxysmal atrial fibrillation in three tertiles of systolic blood pressure

	Candesartan	Amlodipine	P-value
Lower group			
Baseline (day/month)	3.5 ± 3.6 (49)	5.4 ± 6.8 (59)	0.081
Final follow-up	1.7 ± 2.7 (48)	3.1 ± 4.9 (58)	0.089
Difference	−1.6 ± 4.4 (48)	−2.4 ± 7.5 (58)	0.493
Middle group			
Baseline	3.5 ± 5.7 (42)	4.8 ± 6.5 (52)	0.306
Final follow-up	2.6 ± 5.4 (41)	2.7 ± 5.3 (51)	0.928
Difference	−1.0 ± 4.8 (41)	−2.2 ± 5.5 (51)	0.260
Higher group			
Baseline	3.9 ± 4.6 (61)	3.9 ± 5.2 (43)	0.936
Final follow-up	2.1 ± 3.3 (57)	1.3 ± 2.4 (44)	0.164
Difference	−1.7 ± 3.8 (57)	−2.6 ± 4.2 (43)	0.265

Data represent mean ± SD. ( ), number of patients.

Figure 2 (A) Difference in the frequency of atrial fibrillation (days/month) between the observation period and the final month of the follow-up (Left: Total atrial fibrillation, Right: Symptomatic atrial fibrillation). Both in the candesartan (angiotensin II-receptor blocker) and amlodipine (calcium channel blocker) groups, the atrial fibrillation days decreased, but there were no significant differences between the two groups. (B) The time-course of the frequency (days/month) of total atrial fibrillation (dotted lines) and symptomatic atrial fibrillation (solid lines).

with AF.[18–20] Actually, a series of clinical studies also showed that RAS inhibition had beneficial effects on the recurrence and perpetuation of AF.[21–23] On the contrary, however, *post hoc* analyses of the AFFIRM (Atrial Fibrillation Follow-Up Investigation of Rhythm Management) and CTAF (Canadian Trial of Atrial Fibrillation) studies could not find any beneficial effects of RAS inhibition on AF recurrence,[24,25] making it controversial that the experimental concept can be applied to clinical practice.

Recently, the first prospective randomized control trial, the GISSI-AF study,[13] challenged this issue. The trial enrolled all types of AF, evaluated the antiarrhythmic efficacy of valsartan

when compared with a placebo in a double-blind manner, and has demonstrated that valsartan was not associated with any beneficial effects on AF recurrence. Also, the results were consistent in any subgroups according to age, presence of heart failure, and usage of ACE-inhibitors, beta-blockers and antiarrhythmic drugs.[13]

The present J-RHYTHM II study focused upon a specific proportion of patients in the GISSI-AF study, patients with frequent paroxysmal AF associated with hypertension, in order to answer a question regarding which type of drug, ARB or CCB, is more favourable as an anti-hypertensive therapy for these patients. The primary endpoint was also somewhat different from the GISSI-AF study. We focused on the frequency of paroxysmal AF, while the GISSI-AF trial evaluated the time to a first recurrence of AF. Our study, using every-day TTM recordings, has revealed that anti-hypertensive therapy with candesartan has no significant advantage over amlodipine in the reduction in the frequency of paroxysmal AF. These results would strengthen the evidence from the GISSI-AF study.

In our secondary endpoint analysis, ~12% of the patients showed progression into persistent AF. This figure is consistent with a recent study[26] that revealed the rate of progression of paroxysmal into persistent AF in a variety of paroxysmal AF patients and identified hypertension as one of the potent risk factors for AF perpetuation. In the present study, we ascertained the similar progression rate in hypertensive patients with the use of daily TTM recordings and also found that the rate was not significantly affected by the administration of candesartan in a sample size of >300 patients. The changes in the left atrial dimension were also similar between the groups, which would be consistent with this result on AF perpetuation. The present results of the AF-specific QOL assessment are also plausible, because the frequency and perpetuation of AF was similar between the groups.

In our study, the incidence of thrombo-embolic events tended to be higher in the amlodipine than in the candesartan group. This might be inconsistent with the GISSI-AF study,[13] where strokes were more frequently observed in the valsartan group. However, we believe that our observation may have resulted from a by-chance occurrence due to the small number of patients studied.

Recently, several reports have been made on the relationships between anti-hypertensive drugs and AF primary prevention.[27–29] The effects of antihypertensive drugs on primary AF prevention might differ from drug to drug, but remain a matter of controversy. One of the difficult problems results from BP differences during long anti-hypertensive therapy.[30,31] Similarly, the present results could be influenced by the significant differences in BP between the two groups. However, the AF frequencies were not different between ARB and CCB in any of the subgroups divided according to the attained BP levels at the final follow-up: this *post hoc* analysis would suggest that the BP differences between the two groups were unlikely to play a major role in the results of the present study.

Limitations of our trial should include (i) it is an open-label trial, (ii) lack of a placebo arm, (iii) relatively higher rate of antiarrhythmic drug usage in the amlodipine group, and (iv) a relatively short follow-up period. Although this was an open-label trial, the primary endpoint was blinded to the attending physicians and patients, and also to the TTM diagnosis committee, in order to

minimize information biases. Because there was no placebo control group, we could not know the relationships between BP and the frequency of paroxysmal AF. The slightly higher rates of antiarrhythmic drug usage in the amlodipine group (the difference was statistically insignificant) might have affected the present results. Moreover, our results should be applied to a short-term follow-up of the patients.

In conclusion, under the conditions of the study and with statistical limitations, there were no differences in the frequency or perpetuation of paroxysmal AF with hypertension between anti-hypertensive therapies using candesartan and amlodipine. These data suggest that, for both patients and health-care providers, selection of anti-hypertensive drugs could be individualized from other patient characteristics.

Conflict of interest: none declared.

Appendix 1

Takeshi Yamashita: The Cardiovascular Institute, Tokyo, Japan; Hiroshi Inoue: 2nd Department of Internal Medicine, University of Toyama, Toyama, Japan; Ken Okumura: Cardiology, Hirosaki University, Hirosaki, Japan; Itsuo Kodama: Cardiovascular Research, Research Institute of Environmental Medicine, Nagoya University, Nagoya, Japan; Yoshifusa Aizawa: Division of Cardiology, Niigata University Graduate School of Medical and Dental Science, Niigata, Japan; Hirotsugu Atarashi: Internal Medicine, Nippon Medical School Tama-Nagayama Hospital, Tama, Japan; Tohru Ohe: The Sakakibara Heart institute of Okayama, Okayama, Japan; Hiroshi Ohtsu: Clinical Epidemiology and Systems, University of Tokyo, Tokyo, Japan; Takao Katoh: Internal Medicine, Nippon Medical School, Tokyo, Japan; Shiro Kamakura: Cardiovascular Medicine, National Cardiovascular Center, Suita, Japan; Koichiro Kumagai: Fukuoka Sannno Hospital, Fukuoka, Japan; Yoshihisa Kurachi: Department of Pharmacology II, Osaka University, Osaka, Japan; Yukihiro Koretsune: Institute for Clinical Research, Osaka National Hospital, Osaka, Japan; Tetsunori Saikawa: Cardiovascular Science, Oita University, Oita, Japan; Masayuki Sakurai: Department of Cardiology, Hokko Memorial Hospital, Sapporo, Japan; Toshiaki Sato: Department of Cardiology, Keio University, Tokyo, Japan; Kaoru Sugi: Division of Cardiovascular Medicine, Toho University Ohashi Medical Center, Tokyo, Japan; Haruaki Nakaya: Department of Pharmacology, Chiba University, Chiba, Japan; Makoto Hirai: Health Sciences, Nagoya University, Nagoya, Japan; Atsushi Hirayama: Department of Internal Medicine, Nihon University; Masahiko Fukatani: Chikamori Hospital, Kochi, Japan; Hideo Mitamura: Cardiology, Saiseikai Central Hospital, Tokyo, Japan; Tsutomu Yamazaki: Clinical Epidemiology and Systems, University of Tokyo, Tokyo, Japan; Eiichi Watanabe: Division of Cardiology, Department of Internal Medicine, Fujita Health University School of Medicine, Toyoake, Japan; Satoshi Ogawa: IUHW Mita Hospital, Tokyo, Japan.

Appendix 2

J-RHYTHM II Steering Committee: Ogawa S, Aizawa Y, Atarashi H, Inoue H, Ohe T, Okumura K, Hirayama A, Katoh T, Kamakura S, Kumagai K, Kurachi Y, Kodama I, Koretsune Y, Ohtsu H, Saikawa

T. Sakurai M. Sugi K. Nakaya H. Hirai M. Fukatani M. Mitamura H. Yamashita T. Yamazaki T. Watanabe E.

J-RHYTHM II Writing Committee: Yamashita T, Inoue H, Okumura K, Kodama I.

J-RHYTHM II TTM Diagnosis Committee: Sato T, Atarashi H, Ogawa S, Mitamura H, Yamashita T.

J-RHYTHM II Investigators: Katoh T, Igawa O, Matsumoto N, Yamashita T, Kaneko Y, Watanabe E, Ogawa S, Osaka T, Fujii E. Niwano S, Yoshioka K, Kato M, Okazaki O, Kusano K, Okuyama Y, Furushima H, Suzuki M, Noda T, Kawara T, Sato T, Kamakura S, Endoh Y, Kumagai K, Hiyoshi Y, Ishiyama T, Ohtsuka T. Matsumoto M. Chishaki A, Shinohara T, Shirayama T, Koretsune Y, Yokoyama E, Ajiki K, Fujio K, Sugi K, Yamakawa T, Yusu S, Inoue H. Kawamura Y, Hayano M, Date T, Mizusawa Y, Kobayashi Y, Satomi K, Imai Y, Atarashi H, Fukunami M, Yokoshiki H, Betsuyaku T, Okumura K, Takeda H, Matsumoto K, Okishige K, Tagawa M, Hirai M. Okazaki H.

References

1. Wolf PA, Mitchell JB, Baker CS, Kannel WB, D'Agostino RB. Impact of atrial fibrillation on mortality, stroke, and medical costs. *Arch Intern Med* 1998;**158**: 229 34.

2. Benjamin EJ, Wolf PA, D'Agostino RB, Silbershatz H, Kannel WB, Levy D. Impact of atrial fibrillation on the risk of death: the Framingham Heart Study. *Circulation* 1998;**98**:946–52.

3. Wang TJ, Larson MG, Levy D, Vasan RS, Leip EP, Wolf PA et al. Temporal relations of atrial fibrillation and congestive heart failure and their joint influence on mortality: the Framingham Heart Study. *Circulation* 2003;**107**:2920- 25.

4. Wyse DG, Waldo AL, DiMarco JP, Domanski MJ, Rosenberg Y, Schron EB et al. Atrial Fibrillation Follow-up Investigation of Rhythm Management (AFFIRM) Investigators. A comparison of rate control and rhythm control in patients with atrial fibrillation. *N Engl J Med* 2002;**347**:1825- 33.

5. Van Gelder IC, Hagens VE, Bosker HA, Kingma JH, Kamp O, Kingma T et al. Rate Control versus Electrical Cardioversion for Persistent Atrial Fibrillation Study Group. A comparison of rate control and rhythm control in patients with recurrent persistent atrial fibrillation. *N Engl J Med* 2002;**347**:1834- 40.

6. Members of the Sicilian Gambit. New approaches to antiarrhythmic therapy, Part I: emerging therapeutic applications of the cell biology of cardiac arrhythmias. *Circulation* 2001;**104**:2865–73.

7. Lévy S. Drug insight: angiotensin-converting-enzyme inhibitors and atrial fibrillation: indications and contraindications. *Nat Clin Pract Cardiovasc Med* 2006;**3**: 220–5.

8. Patlolla V, Alsheikh-Ali AA, Al-Ahmad AM. The renin-angiotensin system: a therapeutic target in atrial fibrillation. *Pacing Clin Electrophysiol* 2006;**29**: 1006-12.

9. Makkar KM, Sanoski CA, Spinler SA. Role of angiotensin-converting enzyme inhibitors, angiotensin II receptor blockers, and aldosterone antagonists in the prevention of atrial and ventricular arrhythmias. *Pharmacotherapy* 2009;**29**: 31 48.

10. Healey JS, Baranchuk A, Crystal E, Morillo CA, Garfinkle M, Yusuf S et al. Prevention of atrial fibrillation with angiotensin-converting enzyme inhibitors and angiotensin receptor blockers: a meta-analysis. *J Am Coll Cardiol* 2005;**45**:1832–9.

11. Anand K, Mooss AN, Hee TT, Mohiuddin SM. Meta-analysis: inhibition of renin-angiotensin system prevents new-onset atrial fibrillation. *Am Heart J* 2006; **152**:217 22.

12. Schneider MP, Hua TA, Bohm M, Wachtell K, Kjeldsen SE, Schmieder RE. Prevention of atrial fibrillation by renin-angiotensin system inhibition a meta-analysis. *J Am Coll Cardiol* 2010;**55**:2299- 307.

13. GISSI-AF Investigators, Disertori M, Latini R, Barlera S, Franzosi MG, Staszewsky L, Maggioni AP et al. Valsartan for prevention of recurrent atrial fibrillation. *N Engl J Med* 2009;**360**:1606- 17.

14. Nieuwlaat R, Capucci A, Camm AJ, Olsson SB, Andresen D, Davies DW et al. European Heart Survey Investigators. Atrial fibrillation management: a prospective survey in ESC member countries: the Euro Heart Survey on Atrial Fibrillation. *Eur Heart J* 2005;**26**:2422- 34.

15. Nabauer M, Gerth A, Limbourg T, Schneider S, Oeff M, Kirchhof P et al. The Registry of the German Competence NETwork on Atrial Fibrillation: patient characteristics and initial management. *Europace* 2009;**11**:423- 34.

16. Yamashita T, Ogawa S, Aizawa Y, Atarashi H, Inoue H, Ohe T et al. J-RHYTHM II Investigators. Randomized study of angiotensin II type 1 receptor blocker vs. dihydropiridine calcium antagonist for the treatment of paroxysmal atrial fibrillation in patients with hypertension. *Circ J* 2006;**70**:1318–21.

17. Ogawa S, Yamashita T, Yamazaki T, Aizawa Y, Atarashi H, Inoue H et al. J-RHYTHM Investigators. Optimal treatment strategy for patients with paroxysmal atrial fibrillation: J-RHYTHM Study. *Circ J* 2009;**73**:242- 8.

18. Nakashima H, Kumagai K, Urata H, Gondo N, Ideishi M, Arakawa K. Angiotensin II antagonist prevents electrical remodeling in atrial fibrillation. *Circulation* 2000;**101**: 2612 7.

19. Li D, Shinagawa K, Pang L, Leung TK, Cardin S, Wang Z et al. Effects of angiotensin-converting enzyme inhibition on the development of the atrial fibrillation substrate in dogs with ventricular tachypacing-induced congestive heart failure. *Circulation* 2001;**104**:2608- 14.

20. Kumagai K, Nakashima H, Urata H, Gondo N, Arakawa K, Saku K. Effects of angiotensin II type 1 receptor antagonist on electrical and structural remodeling in atrial fibrillation. *J Am Coll Cardiol* 2003;**41**:2197- 204.

21. Madrid AH, Marin IM, Cervantes CE, Morell EB, Estévez JE, Moreno G et al. Prevention of recurrences in patients with lone atrial fibrillation. The dose-dependent effect of angiotensin II receptor blockers. *J Renin Angiotensin Aldosterone Syst* 2004;**5**:114 20.

22. Fogari R, Derosa G, Ferrari I, Corradi L, Zoppi A, Lazzari P et al. Effect of valsartan and ramipril on atrial fibrillation recurrence and P-wave dispersion in hypertensive patients with recurrent symptomatic lone atrial fibrillation. *Am J Hypertens* 2008; **21**:1034–9.

23. Belluzzi F, Sernesi L, Preti P, Salinaro F, Fonte ML, Perlini S. Prevention of recurrent lone atrial fibrillation by the angiotensin-II converting enzyme inhibitor ramipril in normotensive patients. *J Am Coll Cardiol* 2009;**53**:24- 9.

24. Murray KT, Rottman JN, Arbogast PG, Shemanski L, Primm RK, Campbell WB et al. AFFIRM Investigators. Inhibition of angiotensin II signaling and recurrence of atrial fibrillation in AFFIRM. *Heart Rhythm* 2004;**1**:669–75.

25. Patardy M, Ducharme A, Nattel S, Tardif JC, White M, Racine N et al. CTAF investigators. Absence of protective effect of renin-angiotensin system inhibitors on atrial fibrillation development: insights from the Canadian Trial of Atrial Fibrillation (CTAF). *Can J Cardiol* 2008;**24**:709- 13.

26. de Vos CB, Pisters R, Nieuwlaat R, Prins MH, Tieleman RG, Coelen RJ et al. Progression from paroxysmal to persistent atrial fibrillation clinical correlates and prognosis. *J Am Coll Cardiol* 2010;**55**:725- 31.

27. Haywood LJ, Ford CE, Crow RS, Davis BR, Massie BM, Einhorn PT et al. ALLHAT Collaborative Research Group. Atrial fibrillation at baseline and during follow-up in ALLHAT (Antihypertensive and Lipid-Lowering Treatment to Prevent Heart Attack Trial). *J Am Coll Cardiol* 2009;**54**:2023- 31.

28. Schaer BA, Schneider C, Jick SS, Conen D, Osswald S, Meier CR. Risk for incident atrial fibrillation in patients who receive antihypertensive drugs: a nested case-control study. *Ann Intern Med* 2010;**152**:78- 84.

29. Heckbert SR, Wiggins KL, Glazer NL, Dublin S, Psaty BM, Smith NL et al. Antihypertensive treatment with ACE inhibitors or beta-blockers and risk of incident atrial fibrillation in a general hypertensive population. *Am J Hypertens* 2009;**22**: 538–44.

30. Thomas MC, Dublin S, Kaplan RC, Glazer NL, Lumley T, Longstreth WT Jr et al. Blood pressure control and risk of incident atrial fibrillation. *Am J Hypertens* 2008; **21**:1111- 6.

31. Conen D, Tedrow UB, Koplan BA, G'ynn RJ, Buring JE, Albert CM. Influence of systolic and diastolic blood pressure on the risk of incident atrial fibrillation in women. *Circulation* 2009;**119**:2146–52.

Transmural and apicobasal gradients in repolarization contribute to T-wave genesis in human surface ECG

Jun-ichi Okada,[1] Takumi Washio,[1] Akiko Maehara,[2] Shin-ichi Momomura,[3] Seiryo Sugiura,[4] and Toshiaki Hisada[4]

[1]*Graduate School of Frontier Sciences, University of Tokyo, Chiba, Japan;* [2]*Columbia University Medical Center/Cardiovascular Research Foundation, New York, New York;* [3]*Cardiovascular Division, Jichi Medical University Saitama Medical Center, Saitama;* and [4]*Graduate School of Frontier Sciences, University of Tokyo, Tokyo, Japan*

Okada J, Washio T, Maehara A, Momomura S, Sugiura S, Hisada T. Transmural and apicobasal gradients in repolarization contribute to T-wave genesis in human surface ECG. *Am J Physiol Heart Circ Physiol* 301: H200–H208, 2011. First published April 1, 2011; doi:10.1152/ajpheart.01241.2010.—The cellular basis of the T-wave morphology of surface ECG remains controversial in clinical cardiology. We examined the effect of action potential duration (APD) distribution on T-wave morphology using a realistic model of the human ventricle and torso. We developed a finite-element model of the ventricle consisting of ~26 million elements, including the conduction system, each implemented with the ion current model of cardiomyocytes. This model was embedded in a torso model with distinct organ structures to obtain the standard ECG leads. The APD distribution was changed in the transmural direction by locating the M cells in either the endocardial or epicardial region. We also introduced apicobasal gradients by modifying the ion channel parameters. Both the transmural gradient (with M cells on the endocardial side) and the apicobasal gradient produced positive T waves, although a very large gradient was required for the apicobasal gradient. By contrast, T waves obtained with the transmural gradient were highly symmetric and, therefore, did not represent the true physiological state. Only combination of the transmural and the moderate apicobasal gradients produced physiological T waves in surface ECG. Positive T waves in surface ECG mainly originated from the transmural distribution of APD with M cells on the endocardial side, although the apicobasal gradient was also required to attain the physiological waveform.

electrocardiogram; computer simulation; T wave; body surface map; M cells

DESPITE ITS LONG HISTORY AND worldwide use in clinical cardiology for the diagnosis of various heart diseases, the cellular origin of the ECG waveform is not fully established. In particular, the genesis of the T wave remains controversial, largely because of its implication in arrhythmogenesis (1, 4, 20, 22). The T wave was originally considered to result from the heterogeneity of repolarization of the ventricle in the apicobasal direction (19). However, more recently, the transmural difference (gradient) of repolarization is considered important, as supported by the discovery of M cells isolated from the canine ventricular wall (2, 32). M cells are distributed in the deep subendocardium in the anterior wall, but are shifted to the deep subepicardium in the posterior wall, and are characterized by a longer action potential duration (APD) compared with the epicardial and endocardial myocytes, creating a significant gradient (1). Subsequent studies identified similar type of cells in

guinea pig, rabbit, pig, and human ventricular tissues (8, 33, 35, 51).

However, when measurements are made in more intact preparations, there is accumulating evidence that the APD of M cells becomes shorter, resulting in smaller transmural dispersion (23). For instance, measurement of the human ventricles during cardiac surgery, rather than isolated cells or a ventricular wedge, produced no significant transmural heterogeneity of repolarization (42). The electronic cancellation effect introduced by intercellular coupling through gap junctions is considered the cause of these observations in intact preparations (5, 41), although experimental artifact has also been suggested (1). During surgery or in animal experiments, subjects receive anesthetic agents that may block sodium and/or delayed rectifier potassium currents, causing preferential shortening of the APD of M cells (31). Furthermore, the plunge electrode technique used in many studies may not necessarily probe the whole area and depth of the ventricular wall (42, 48). In a recent study, optical mapping revealed the distribution of APD in human ventricular tissue (12); however, only the posterior wall wedge was examined.

Computer simulation is widely used for studying cardiac electrophysiology and allows detailed analysis of the normal and abnormal electrical activity of the heart (18, 34, 46, 47). Although computer simulation does not provide conclusive data on actual tissue, if carefully designed, it can provide important supporting information. In the present study, we used this strategy to examine which pattern of APD distribution generated the normal waveform of the human surface ECG. We previously reported our detailed model of the human ventricles based on the human ventricular model of electrophysiology (44, 45). We embedded this model into a torso with the organ structures model and varied the distributions of M cells and APD, according to experimental data, to calculate the surface ECG. We found that both the apicobasal and transmural distribution of APD significantly influence the human T-wave morphology.

MATERIALS AND METHODS

Human heart and torso model. The details of this model were previously reported (50). We used a realistic model of the human heart with a conduction system embedded into the torso model based on the voxel-based, finite-element method. To save computational cost for such a large-scale model, we used composite mesh composed of fine mesh (0.2 mm) for the heart and the coarse mesh (1.6 mm) for the torso regions and solved it using the multilevel solution technique. The study protocol was approved by the Institutional Ethics Committee, and informed consent was obtained for the use of CT scan data.

Heart model. The geometry of the three-dimensional voxel human heart model (mesh size 0.2 mm) was based on the multidetector computerized tomography data of the subject without cardiac dysfunction (Fig. 1A). We only analyzed the ventricles, although the total number of elements covering the heart region was equal to 244,187,136. We mapped previously reported human data on the spatial orientation of the myocyte (fiber orientation) to our model (http://gforge.icm.jhu.edu/gf/project/dtmri_data_sets/) (Fig. 1B).

To each voxel element, we implemented the previously reported ionic current model of human ventricular myocytes (45), and the propagation of excitation was modeled as a continuous system using the bidomain formulation (see supplemental material for details; the online version of this article contains supplemental data) (14). Anisotropy of action potential propagation was introduced by setting the conductivity in the longitudinal (fiber) direction larger compared with the transverse direction. We used the following values (Supplemental Table S1), according to the previous report (15).

Conduction system. The conduction system is indispensable for the analysis of ECG. We modeled the conduction system by one-dimensional elements based on Tawara's monograph (43), as shown in Fig. 2A. The electrophysiological properties were reproduced by the cell model proposed by Stewart et al. (36). The network of the conduction system consists of the free-running (insulated) part connecting the atrioventricular node to the sites of earliest activation and the network spreading from these sites along the endocardial surface. At each terminal, this network is connected to the voxel mesh node, representing the myocardial tissue, and from there the excitation propagates concentrically. Although the description by Tawara is qualitative, the current model can be validated by the agreement of simulation results of previously reported isochronal maps (Fig. 2, B and C) (9) and body

surface voltage maps (Fig. 2D) (6, 40). In the simulation, we applied a small current to the root of the conduction system to initiate activation of the ventricles.

Torso model. The morphology of the voxel torso model was based on the computerized tomography data (Fig. 1C). Each organ was segmented manually (Fig. 1D), and specific conductivity (Supplemental Table S1) was assigned as previously reported (3, 21). Only the conductivity of the body surface (skin) was adjusted to obtain the physiological amplitude of ECG without changing its morphology. With a 1.6-mm element size, the total number of elements covering the torso was 40,038,400. In contrast to the heart tissue, the torso domain can be viewed as a passive conductor. Therefore, the potential ϕ^T satisfies the generalized Laplace equation

$$\frac{\partial}{\partial x_i}\left(G_{ij}^T \frac{\partial \phi^T}{\partial x_j}\right) = 0$$

where G_{ij}^T is the conductivity tensor.

APD distribution. We altered the APD distributions (gradients) in transmural and apicobasal (longitudinal) directions to determine the effects on ECG. Using the Ten Tusscher model (45), we found that the endocardial cells, M cells, and epicardial cells were modeled by adjusting the transient outward K^+ and the slow component of delayed rectifier K^+ currents (I_{Ks}). Transmural gradient was created by locating M cells in either the endocardial or epicardial sides (10–40%, Fig. 3A, or 60–90%, Fig. 3B, from the endocardium, respectively). However, regional differences in APD were attenuated due to the intercellular coupling. We also tested conditions with no transmural gradient in which all of the layers were composed of epicardial cells (Fig. 3C). Transmural dispersion of APD, APD
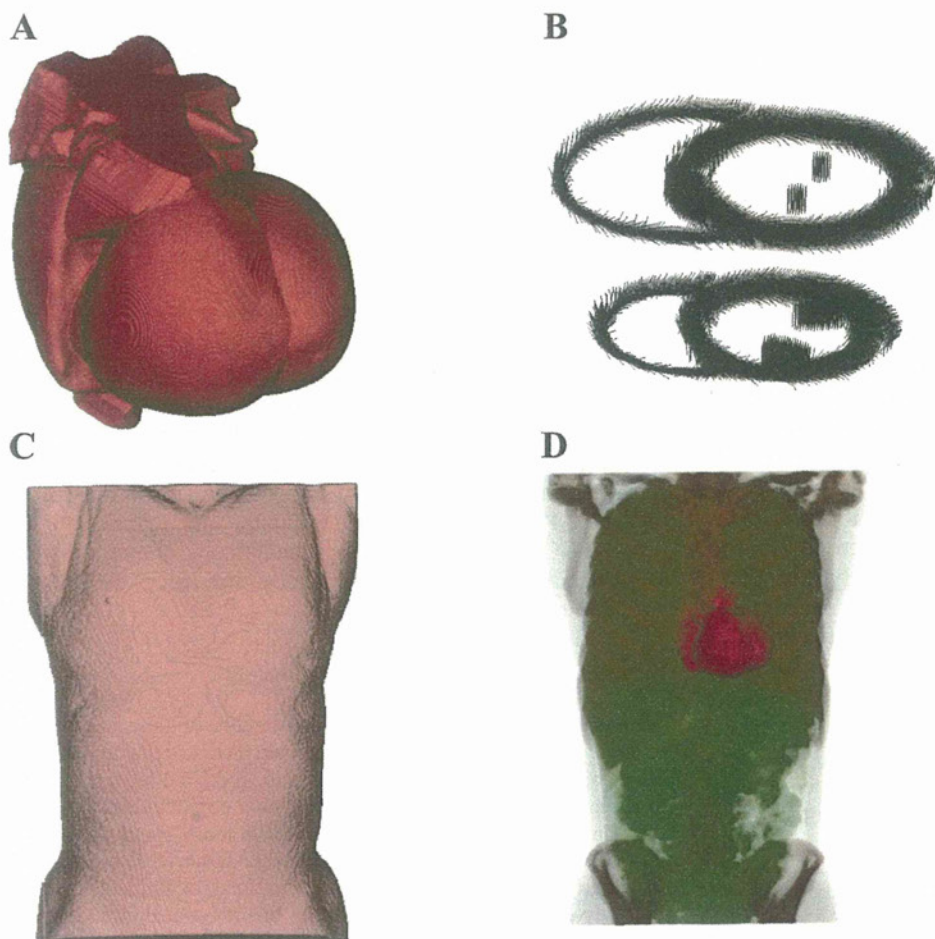
A

B

C

D

Fig. 1. Heart and torso models. A: human heart model with fine mesh. B: fiber directions mapped in the ventricles. C: torso model. D: transparent view showing the organs in the torso model.
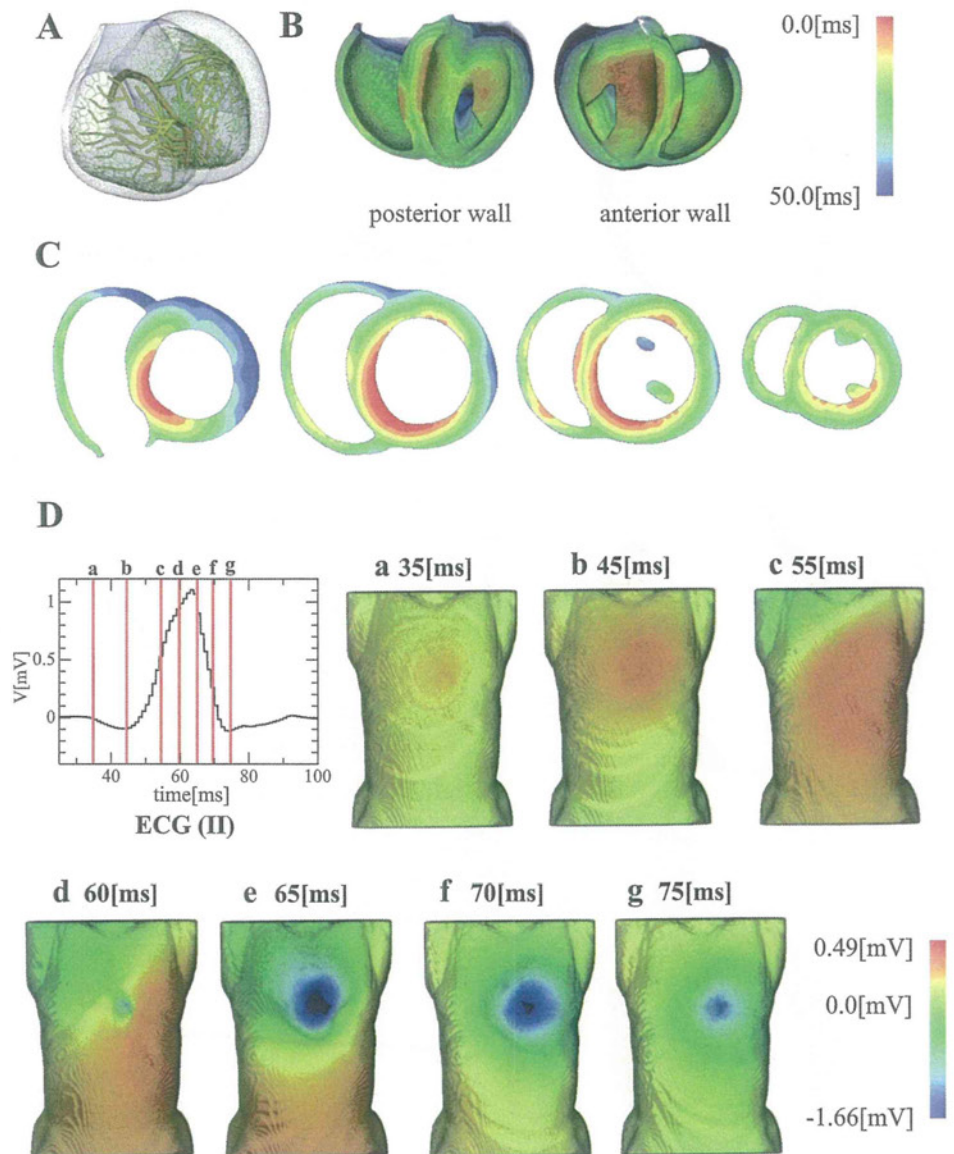
Fig. 2. Conduction system and ventricular activation. *A*: the conduction system with Purkinje fiber network. *B*: cut-out view of the ventricles showing activation sequence in color. *C*: isochronal map of activation in the transverse sections. *D*: sequential maps of the body surface potential during the activation phase. The timing of each map is indicated in the *top left* panel. V, voltage.

gradient, and the conduction velocity in these models are shown and compared with the experimental data (note that the *x*-axes are reversed for canine experimental data in Fig. 3, *D–F*). In Fig. 3*D*, APD distributions are shown for three models. The APD gradient of the model with M cells on the endocardial side (red line) showed general agreement with the canine heart (24), although the experimentally reported epicardial steep APD gradient was not observed in the simulation (Fig. 3*E*). Similarly, the simulation results did not show the epicardial gap in conduction velocity. Poelzing et al. (24) suggested that the epicardial APD gradient and the gap in conduction velocity are due to the heterogeneous expression of connexin 43 (Cx43), which we did not take into considerations in this study. However, the APD distribution reported for the human ventricular wall (12) did not show this epicardial gradient, thus closely resembling our simulation results.

As for the apicobasal gradient, Szentadrassy et al. reported a significant difference in the expression level of proteins forming the I_{Ks} channel between the apical and basal myocardium (38). We observed a similar trend for the transient outward K$^+$ current channel, although the difference in Kv4.3 was not significant. We modeled the apicobasal difference by regionally changing the I_{Ks} density. However, as detailed information on the distribution was not available, we

introduced the linear apicobasal gradient with either 20 or 40% of the basal-to-apical ratio; these values were estimated from reported protein levels of these channels (38). We simulated the ECG for the nine combinations of these transmural and apicobasal APD gradients.

Computation. We used the IBM Blade Center consisting of 336 Power6 (4.0 GHz) processors for computation. The total number of degree of freedom was three hundred million, which took 6 h to calculate a single cardiac cycle.

RESULTS

Ventricular activation. Isochronal maps of ventricular activation are shown in Fig. 2, *B* and *C*, for the condition of endocardial M cells with no apicobasal gradient. As the conduction system was identical, we observed similar isochronal maps in all of the conditions tested; these data were similar to those previously reported (9). The temporal changes in body surface potential during the corresponding phase of ventricular activation (Fig. 2*D*; see also Supplemental Movie S1) were also in good agreement with published studies (6). Further-
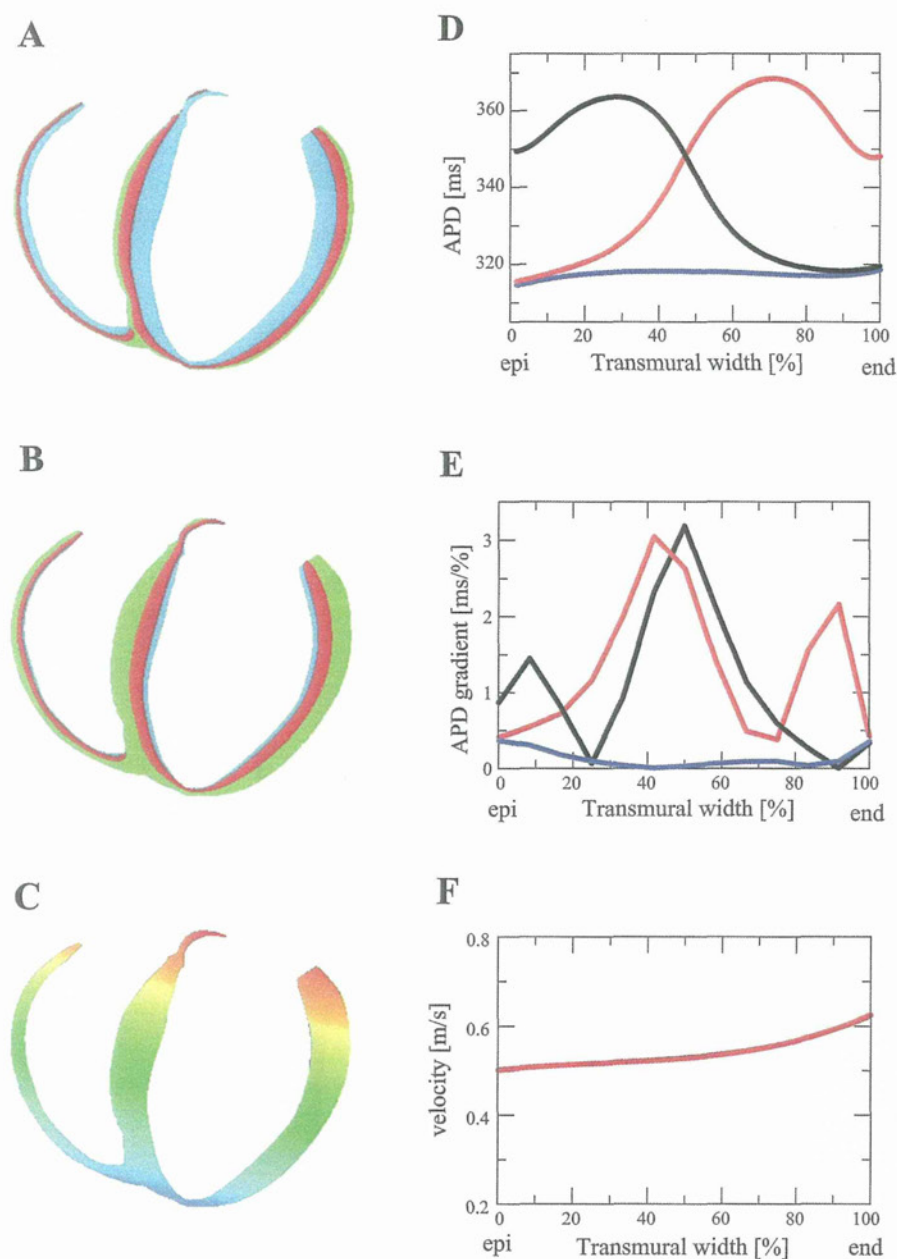
A

D

B

E

Fig. 3. Transmural distributions of M cell, action potential duration (APD), and conduction velocity. A: M cell located on the endocardial side. B: M cell located on the epicardial side. In A and B, the endocardial cell layer is indicated in blue, M cells in red, and epicardial cells in green. C: apicobasal APD gradients are shown in color from red (long) to blue (short). D: transmural ADP dispersion for the model shown in A (red line), B (black line), and C (blue line). E: APD gradient for the three models. Line colors are as in D. F: transmural distribution of conduction velocity.

C

F

more, the QRS complex of surface ECG generated from these body surface maps exhibited a similar standard morphology in all conditions (Fig. 4). Overall, these data indicate the validity of our modeling of the conduction system and also confirms that APD has little effect on the activation sequence in the ventricles.

APD dispersion and T wave. APD dispersion had a significant effect on the morphology of T waves (Fig. 4). In the normal cardiogram, the T waves were typically upright in I, II, and the lateral precordial leads (17), but were all negative in these leads in hearts with M cells on the epicardial side (Fig. 4, *G–I*). Nevertheless, even without the M cells, T waves become upright with a large apicobasal gradient (Fig. 4C). These data suggest that both the transmural (endo- to epicardial) and apicobasal gradients can generate upright T waves in these leads. Indeed, we obtained ECG with upright T waves in the following four conditions: *condition C*, no M cell with 40% apicobasal gradient; *condition D*, endocardial M cell with no

apicobasal gradient; *condition E*, endocardial M cell with 20% apicobasal gradient; and *condition F*, endocardial M cell with 40% apicobasal gradient.

Nevertheless, there were significant differences in the T-wave characteristics between the conditions. In *condition C*, maximum amplitudes of T wave were small in both limbs, with the precordial leads measuring only 0.1 mV in V6. The T waves in the other conditions had a similar peak amplitude, but differed in morphology, particularly in their symmetry. For quantitative comparison, we calculated the asymmetry ratio defined as the ratio of the two areas (beginning-to-peak and peak-to-end) under the T curves of precordial leads for these conditions (Table 1). Asymmetry ratios in *condition C* were all less than unity, confirming the inverse asymmetry of the T waves in this condition. Interestingly, there was an inverse asymmetry (symmetry ratio < 1) in V6 for conditions with endocardial M cells, but without a large apicobasal gradient
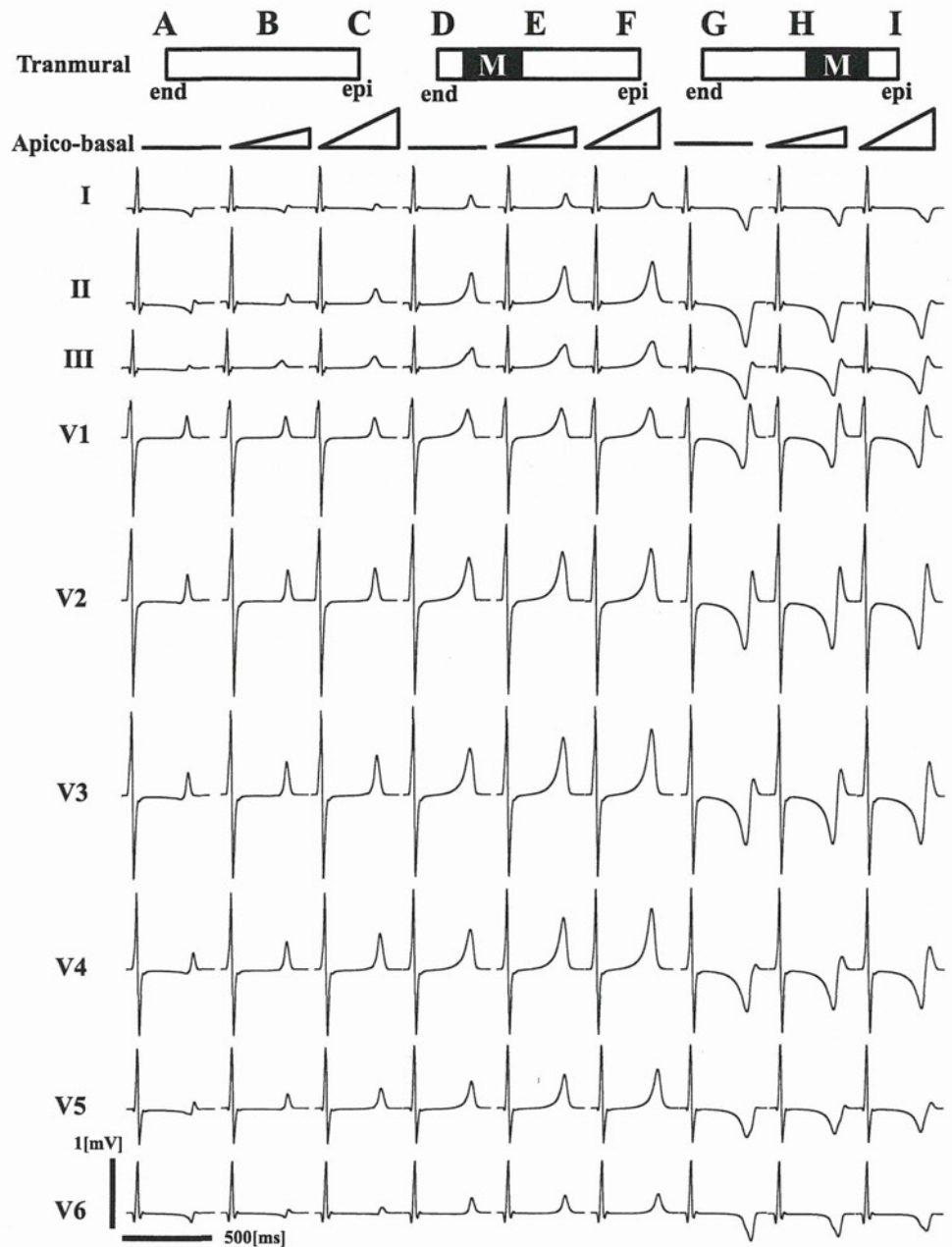
Fig. 4. Electrocardiogram obtained with the nine combinations of the transmural and apicobasal APD gradients. *A, B,* and *C* represent the ECGs with no transmural gradient and varying degree of apicobasal gradients. *D, E,* and *F* represent the ECGs with M cells on the endocardial side and varying degree of apicobasal gradients. *G, H,* and *I* represent the ECGs with M cells on the epicardial side and varying degree of apicobasal gradients.

(*conditions D* and *E*). In healthy subjects, an asymmetry ratio of 1.5 was reported (17), and a correlation between T-wave symmetry and sudden death was suggested. In this regard, we consider that *condition F* may be the most physiological condition for generating a healthy ECG.

Table 1. *Symmetry ratio*

	V2	V3	V4	V5	V6
M cell at endocardium. No apicobasal gradients	1.66	1.74	1.80	1.38	0.70
M cell at endocardium. Apicobasal gradients 20%	1.75	1.76	1.73	1.59	0.94
M cell at endocardium. Apicobasal gradients 40%	1.70	1.70	1.66	1.59	1.02
No M cell. Apicobasal gradients 40%	0.79	0.83	0.96	0.82	0.71

Body surface potential during the repolarization phase. Finally, we compared the body surface potential maps of four conditions (*C, D, E, F*) at the timing of peak T wave, which showed physiological T-wave morphology (Fig. 5) with the previously reported equipotential map of healthy human subjects (39). On the anterior thoracic surface, the positive voltage region of the experimental data (Fig. 3C of Ref. 39) extends down to the lower body, thus resembling *condition F* in our simulation. On the posterior surface, the 0-mV line ran obliquely in the middle of the back so that the positive region was also observed. Taken together, *condition F* showed the closest appearance to the experimental data. The data for different timings can be seen in the Supplemental Movies. Overall, these data suggest that the normal surface ECG waveform cannot be obtained with either transmural or apicobasal gradient of APD alone. Most probably, both contribute to the genesis of surface ECG.

Condition C   **Condition D**   **Condition E**   **Condition F**

-0.15[mV]
0.0[mV]
0.75[mV]
0.5[mV]
0.35[mV]
0.25[mV]
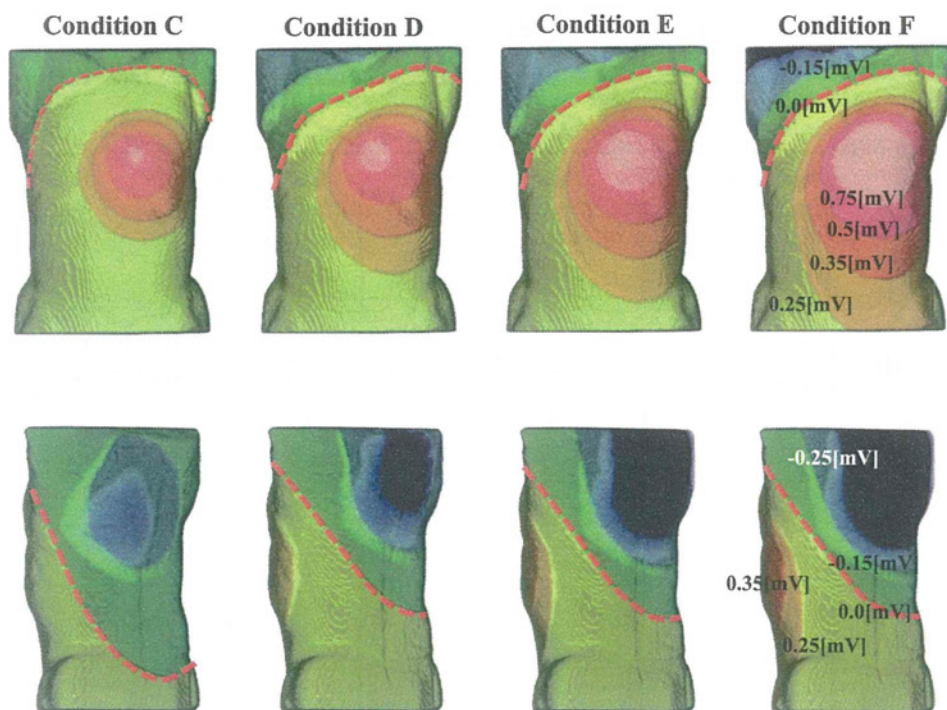
-0.25[mV]
-0.15[mV]
0.35[mV]
0.0[mV]
0.25[mV]

Fig. 5. Body surface potentials at the T-wave peak. *Top* row shows the anterior thoracic surface, and the *bottom* row shows the posterior surface of the results obtained with *models C, D, E,* and *F,* from *left* to *right.* Red dashed lines indicate the 0-mV line.

DISCUSSION

Computer simulation is a powerful tool in cardiac electrophysiology studies. Various models have been used to examine ECG wave morphology, although studies typically treat either a small number of cell models coupled in series (5, 10, 25) or a tissue block (wedge) (7, 26). Recently, an ionic current model based on large-scale simulation of the heart was developed, although studies using this model are either without the torso (27) or do not examine physiological conduction (52). To the best of our knowledge, this is the first report where surface ECG was simulated based on the ionic current model and anisotropic propagation with the bidomain reaction diffusion equation in a model with realistic morphology of the human torso and heart.

APD dispersion and T-wave morphology. The results of our simulation suggest that the physiological morphologies of T waves are generated mainly by the transmural distribution of APD, although the contribution of the apicobasal gradient is also important. Although recent studies suggest that the cancellation effect in the intact heart can minimize transmural dispersion (5, 41, 42), a large apicobasal gradient is required to observe positive T waves in limb and left precordial leads under such conditions (Fig. 4C). Even when using a relatively large apicobasal gradient we could only obtain a highly symmetric, thus nonphysiological, T-wave morphology. Furthermore, the amplitude of the T wave in V6 was very small and symmetric in shape only with the transmural gradient, which is also a nonphysiological morphology.

Recently, experimental evidence of a transmural APD gradient was reported in the human heart (12). However, in contrast to animal data (mainly from electrode recordings), two-dimensional mapping in this study identified M cells clustering in an isolated island, rather than forming a contiguous layer, in 60% of nonfailing ventricular wedge preparations. Furthermore, although the number of samples was limited, that study may suggest the presence of an apicobasal

gradient, because these islands were shifted to the basal end in most of the graphs. We simulated the effect of uneven M-cell distribution by reducing the fraction of the M-cell region in the apex. Furthermore, as the data from Glukhov et al. (12) were only taken from a limited region of the left ventricular (LV) wall, we used the smooth apicobasal distribution of M cells and obtained a physiological ECG.

Regional differences. The effect of APD gradient differed among the different leads (see Fig. 6). In the absence of
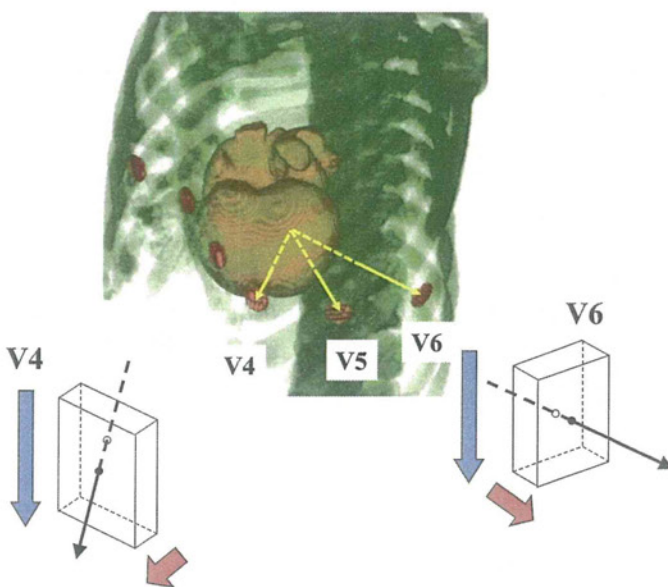

Fig. 6. Diagram showing the effect of lead position on T-wave morphology. The line connecting the V6 lead and the hypothetical zero point crosses the ventricular wall perpendicularly so that the T wave mainly reflects the transverse APD gradient (red arrow). The line connecting the V4 lead and the zero point crosses the wall at an oblique angle so that the T wave is influenced by both transverse (red) and apicobasal gradients (blue arrow).

transmural gradient, the amplitude of the T wave in V6 was small and relatively indifferent to the apicobasal gradient. In a previous study that recorded transmural ECG at 0, 45, −45, and 90° angles relative to the transmural axis, the amplitude of the T wave was highly dependent on the angle and peaked at 0° (53). If we assume that the reference electrode (putative 0 potential) is in the center of the LV, the line connecting this electrode and the V6 lead crosses the LV wall in almost a perpendicular manner and also becomes perpendicular to the apicobasal gradient. On the other hand, because the lines connecting V3 or V4 cross the wall at a shallow angle, T-wave amplitudes are sensitive to the apicobasal gradient. A similar logic may apply to the effect of the transmural gradient when comparing T waves in V5 and V6 among the three conditions without apicobasal gradient. These T waves were either nearly flat, positive, or simply negative (monophasic), thus faithfully

reflecting the transmural gradient. Although genesis of surface ECG is not this simple, useful information on APD distribution may be obtained from these comparisons.

Study limitations. Although our simulation faithfully reproduced the physiological ECG waveform, multiple factors needed to be included in our model for further improvement. First, considering the anisotropy in conduction property of the myocardial tissue, the fiber orientation could have a significant impact on the ECG morphology. To examine this possibility, we compared the ECGs obtained with either human (http://gforge.icm.jhu.edu/gf/project/dtmri_data_sets/) or rabbit (30) fiber orientation (Fig. 7) and found no appreciable difference between them. However, as there are numerous reports indicating the deviations of fiber orientation in diseased hearts (13, 16), further studies are required. Second, in this simulation, the APD gradient was introduced by the heterogeneous expression of K^+ channels based on the ad-
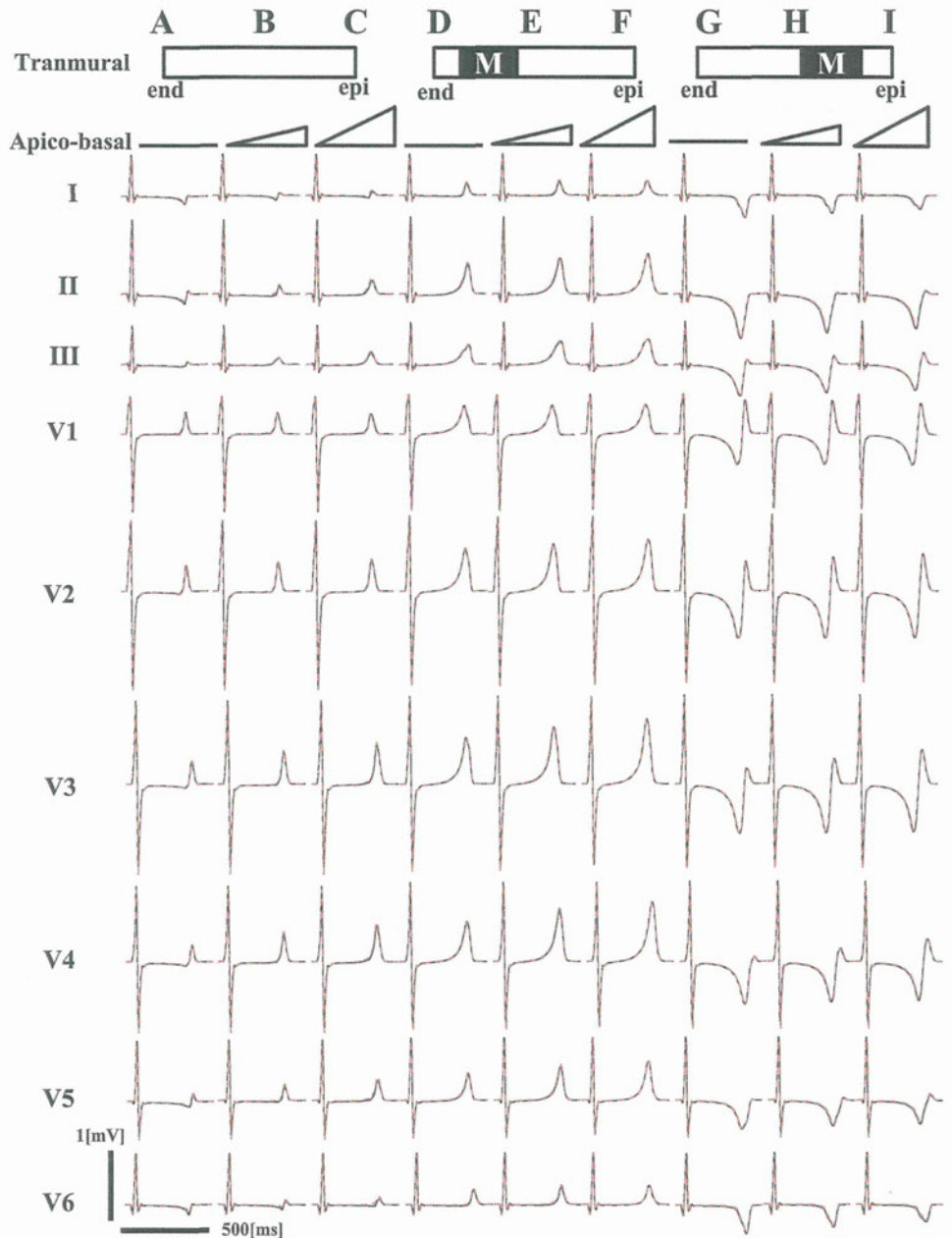

Fig. 7. The ECGs simulated with either human (black line) or rabbit (red line) fiber orientations.

opted cell models (44). However, other molecules are also expressed heterogeneously and thus contribute to the transmural APD gradient. For example, Poelzing et al. (24) reported significantly lower Cx43 expression in the subepicardial layer of the canine LV. Furthermore, downregulation of Cx43 was correlated with the short APD and conduction velocity in this layer. More recently, Poelzing et al. also showed that such heterogeneity in Cx43 expression is significant in anterior LV, and that the poster region lacking Cx43 heterogeneity exhibits flat APD distribution across the wall (37). A similar Cx43 downregulation was reported in the epicardial layer in the human ventricles (12). However, they also showed some discrepancies with the canine heart: *1*) although they studied only the posterior-lateral part of the LV, a significant difference in Cx43 expression was observed transmurally; *2*) although the number of observations was limited, the APD distribution did not show the steep gradient in the epicardial region as shown in the canine heart; and *3*) downregulation of Cx43 in failing human heart resulted in the reduction of local and global transmural APD gradient, thus showing clear contrast to the animal study. Because of these discrepancies between the studies and the lack of information on the whole ventricle, we did not include the effect of Cx43 and only examined effect of the different cell species in our study.

In addition to Cx43, various other ion channels and exchangers are expressed heterogeneously across the ventricular wall. For example, the protein levels of sarco(endo)plasmic reticulum Ca^{2+}-ATPase 2 and ryanodine receptor channel are reduced, whereas the Na/Ca exchanger is upregulated, in the endocardium of the guinea pig ventricle (49). Furthermore, although the number of specimens was small, sarco(endo)plasmic reticulum Ca^{2+}-ATPase 2 mRNA levels were downregulated in endocardial tissue, while Na/Ca exchanger expression was comparable to the epicardial tissue obtained from the human heart (28). Transmural heterogeneity was also reported for the late component of Na currents (29, 54) and the Na-K pump (11). Although APD is influenced by the complex interplay of currents and ion concentrations mediated by these molecules, inclusion of these changes to the model may not drastically change the simulation results, as long as the longer APD is distributed to the endocardial side. Nevertheless, further analysis including these factors is required. Finally, the ST segments in our model appeared to be unusually flat rather than being upslope in some leads. This was likely caused by the flat plateau phase of action potential generated by the ion current model we used (44, 45).

REFERENCES

1. **Antzelevitch C.** Transmural dispersion of repolarization and the T wave. *Cardiovasc Res* 50: 426–431, 2001.
2. **Antzelevitch C, Simizu W, Yan GX, Weissenburger J, Nesterenko VV, Burashnikov A, DiDiego JM, Saffitz JE, Thomas GP.** The M cell: its contribution to the ECG and to normal and abnormal electrical function. *J Cardiovasc Electrophysiol* 10: 1124–1152, 1999.
3. **Camacho MA, Lehr JL, Eisenberg SR.** A three-dimensional finite element model of human transthoracic defibrillation: paddle placement and size. *IEEE Trans Biomed Eng* 42: 572–578, 1995.
4. **Conrath CE, Opthof T.** Ventricular repolarization: an overview of (patho)physiology, sympathetic effects and genetic aspects. *Prog Biophys Mol Biol* 92: 269–307, 2006.
5. **Conrath CE, Wilders R, Coronel R, de Bakker JMT, Taggart P, de Groot JR, Opthof T.** Intercellular coupling through gap junctions masks M cells in the human heart. *Cardiovasc Res* 62: 407–414, 2004.
6. **De Ambroggi L, Taccardi B, Macchi E.** Body-surface maps of heart potentials: tentative localization of pre-excited areas in forty-two Wolff-Parkinson-White patients. *Circulation* 54: 251–263, 1976.
7. **Dos Santos RW, Otaviano Campos F, Neumann Ciuffo L, Nygren A, Giles W, Koch H.** ATX-II effects on the apparent location of M cells in a computational model of a human left ventricular wedge. *J Cardiovasc Electrophysiol* 17: S86–S95, 2006.
8. **Drouin E, Charpentier F, Gauthier C, Laurent K, Le Marec H.** Electrophysiologic characteristics of cells spanning the left ventricular wall of human heart: evidence for presence of M cells. *J Am Coll Cardiol* 26: 185–192, 1995.
9. **Durrer D, van Dam RT, Freud GE, Janse MJ, Meijler FL, Arzbaecher RC.** Total excitation of the isolated human heart. *Circulation* 41: 899–912, 1970.
10. **Fish JM, Di Diego JM, Nesterenko V, Antzelevitch C.** Epicardial activation of left ventricular wall prolongs QT interval and transmural dispersion of repolarization implications for biventricular pacing. *Circulation* 109: 2136–2142, 2004.
11. **Gao J, Wang W, Cohen IS, Mathias RT.** Transmural gradients in Na/K pump activity and [Na⁺]I in canine ventricle. *Biophys J* 89: 1700–1709 2005.
12. **Glukhov AV, Fedorov VV, Lou Q, Ravikumar VK, Kalish PW, Schuessler RB, Moazami N, Efimov IR.** Transmural dispersion of repolarization in failing and nonfailing human ventricle. *Circ Res* 106: 981–991, 2010.
13. **Helm PA, Younes L, Beg MF, Ennis DB, Leclercq C, Faris OP, McVeigh E, Kass D, Miller MI, Winslow RL.** Evidence of structural remodeling in the dyssynchronous failing heart. *Circ Res* 98: 125–132, 2006.
14. **Henriquez CS.** Simulating the electrical behavior of cardiac tissue using the bidomain model. *Crit Rev Biomed Eng* 21: 1–77, 1993.
15. **Keldermann RH, ten Tusscher KH, Nash MP, Bradley CP, Hren R, Taggart P, Panfilov AV.** A computational study of mother rotor VF in the human ventricles. *Am J Physiol Heart Circ Physiol* 296: H370–H379, 2009.
16. **Maron BJ.** Hypertrophic cardiomyopathy. *Curr Probl Cardiol* 18: 641–704, 1993.
17. **Mirvis DM, Goldberger AL.** Electrocardiography. In: *Heart Disease*, edited by Braunwald E, Zipes DP, and Libby P. Philadelphia, PA: Saunders, 2001, p. 82–125.
18. **Noble D.** From the Hodgkin-Huxley axon to the virtual heart. *J Physiol* 580: 15–22, 2007.
19. **Noble D, Cohen I.** The interpretation of the T wave of the electrocardiogram. *Cardiovasc Res* 12: 13–27, 1978.
20. **Opthof T, Coronel R, Janse MJ.** Is there a significant transmural gradient in repolarization time in the intact heart?: Repolarization gradients in the intact heart. *Circ Arrhythm Electrophysiol* 2: 89–96, 2009.
21. **Panescu D, Webster JG, Tompkins WJ, Stratbucker RA.** Optimization of cardiac defibrillation by three-dimensional finite element modeling of the human thorax. *IEEE Trans Biomed Eng* 42: 185–192, 1995.
22. **Patel C, Burke JF, Patel H, Gupta P, Kowey PR, Antzelevitch C, Yan GX.** Is there a significant transmural gradient in repolarization time in the intact heart?: Cellular basis of the T wave: a century of controversy. *Circ Arrhythm Electrophysiol* 2: 80–88, 2009.

23. **Poelzing S.** Are electrophysiologically distinct M-cells a characteristic of the wedge preparation? *Heart Rhythm* 6: 1035–1037, 2009.

24. **Poelzing S, Akar FG, Baron E, Rosenbaum DS.** Heterogeneous connexin43 expression produces electrophysiological heterogeneities across ventricular wall. *Am J Physiol Heart Circ Physiol* 286: H2001–H2009, 2004.

25. **Potse M, Coronel R, Opthof T, Vinet A.** Simulating T-wave parameters of local extracellular electrograms with a whole-heart bidomain reaction-diffusion model: Size matters! *Conf Proc IEEE Eng Med Biol Soc* 2007: 6644–6647, 2007.

26. **Potse M, Dubé B, Richer J, Vinet A, Gulrajani RM.** A comparison of monodomain and bidomain reaction-diffusion models for action potential propagation in the human heart. *IEEE Trans Biomed Eng* 53: 2425–2435, 2006.

27. **Potse M, Vinet A, Opthof T, Coronel R.** Validation of a simple model for the morphology of the T wave in unipolar electrograms. *Am J Physiol Heart Circ Physiol* 297: H792–H801, 2009.

28. **Prestle J, Dieterich S, Preuss M, Bieligk U, Hasenfuss G.** Heterogeneous transmural gene expression of calcium-handling proteins and natriuretic peptides in the failing human heart. *Cardiovasc Res* 43: 323–331, 1999.

29. **Sakmann BFAS, Spindler AJ, Bryant SM, Linz KW, Noble D.** Distribution of a persistent sodium current across the ventricular wall in guinea pig. *Circ Res* 87: 910–914, 2000.

30. **Scollan DF, Holmes A, Winslow R, Forder J.** Histological validation of myocardial microstructure obtained from diffusion tensor magnetic resonance imaging. *Am J Physiol Heart Circ Physiol* 275: H2308–H2318, 1998.

31. **Shimizu W, McMahon B, Antzelevitch C.** Sodium pentobarbital reduces transmural dispersion of repolarization and prevents torsades de Pointes in models of acquired and congenital long QT syndrome. *J Cardiovasc Electrophysiol* 10: 154–164, 1999.

32. **Sicouri S, Antzelevitch C.** A subpopulation of cells with unique electrophysiological properties in the deep subepicardium of the canine ventricle. The M cell. *Circ Res* 68: 1729–1741, 1991.

33. **Sicouri S, Quist M, Antzelevitch C.** Evidence for the presence of M cells in the guinea pig ventricle. *J Cardiovasc Electrophysiol* 7: 503–511, 1996.

34. **Silva JR, Pan H, Wu D, Nekouzadeh A, Decker KF, Cui J, Baker NA, Sept D, Rudy Y.** A multiscale model linking ion-channel molecular dynamics and electrostatics to the cardiac action potential. *Proc Natl Acad Sci USA* 106: 11102–11106, 2009.

35. **Stankovicova T, Szilard M, De Scheerder I, Spido KR.** M cells and transmural heterogeneity of action potential configuration in myocytes from the left ventricular wall of the pig heart. *Cardiovasc Res* 45: 952–960, 2000.

36. **Stewart P, Aslanidi OV, Noble D, Noble PJ, Boyett MR, Zhang H.** Mathematical models of the electrical action potential of Purkinje fibre cells. *Philos Transact A Math Phys Eng Sci* 367: 2225–2255, 2009.

37. **Strom M, Wan X, Poelzing S, Ficker E, Rosenbaum DS.** Gap junction heterogeneity as mechanism for electrophysiologically distinct properties across the ventricular wall. *Am J Physiol Heart Circ Physiol* 298: H787–H794, 2010.

38. **Szentadrassy N, Banyasz T, Biro T, Szabo G, Toth BI, Magyar J, Lazar J, Varro A, Kovacs L, Nanasi PP.** Apico-basal inhomogeneity in distribution of ion channels in canine and human ventricular myocardium. *Cardiovasc Res* 65: 851–860, 2005.

39. **Taccardi B.** Body surface distribution of equipotential lines during atrial depolarization and ventricular repolarization. *Circ Res* 19: 865–878, 1966.

40. **Taccardi B.** Distribution of heart potentials on the thoracic surface of normal human subjects. *Circ Res* 12: 341–352, 1963.

41. **Taggart P, Sutton P, Opthof T, Coronel R, Kallis P.** Electrotonic cancellation of transmural electrical gradients in the left ventricle in man. *Prog Biophys Mol Biol* 82: 243–254, 2003.

42. **Taggart P, Sutton PM, Opthof T, Coronel R, Trimlett R, Pugsley W, Kallis P.** Transmural repolarization in the left ventricle in humans during normoxia and ischaemia. *Cardiovasc Res* 50: 454–462, 2001.

43. **Tawara S.** *Das Reizleitungssystem des Säugetierherzen: Eine anatomisch-histologische Studie uber das Atrioventrikularbundel und die Purkinjeschen Faden.* Jena, Germany: Gustav Fischer, 1906.

44. **Ten Tusscher KH, Noble D, Noble PJ, Panfilov AV.** A model for human ventricular tissue. *Am J Physiol Heart Circ Physiol* 286: H1573–H1589, 2004.

45. **Ten Tusscher KH, Panfilov AV.** Alternans and spiral breakup in a human ventricular tissue model. *Am J Physiol Heart Circ Physiol* 291: H1088–H1100, 2006.

46. **Trayanova NA.** Whole-heart modeling: applications to cardiac electrophysiology and electromechanics. *Circ Res* 108: 113–128, 2011.

47. **Vigmond E, Vadakkumpadan F, Gurev V, Arevalo H, Deo M, Plank G, Trayanova N.** Towards predictive modelling of the electrophysiology of the heart. *Exp Physiol* 94: 563–577, 2009.

48. **Voss F, Opthof T, Marker J, Bauer A, Katus HA, Becker R.** There is no transmural heterogeneity in an index of action potential duration in the canine left ventricle. *Heart Rhythm* 6: 1028–1034, 2009.

49. **Wan X, Laurita KR, Pruvot EJ, Rosenbaum DS.** Molecular correlates of repolarization alternans in cardiac myocytes. *J Mol Cell Cardiol* 39: 419–428, 2005.

50. **Washio T, Okada J, Hisada T.** A parallel multilevel technique for solving the bidomain equation on a human heart with Purkinje fibers and a torso model. *SIAM Review* 52: 717–743, 2010.

51. **Weirich J, Bernhardt R, Loewen N, Wenzel W, Antoni H.** Regional and species-dependent effects of K$^+$-channel blocking agents on subendocardium and mid wall slices of human, rabbit and guinea pig myocardium (Abstract). *Pflügers Arch* 431: R130, 1996.

52. **Xue J, Gao W, Chen Y, Han X.** Study of repolarization heterogeneity and electrocardiographic morphology with a modeling approach. *J Electrocardiol* 41: 581–587, 2008.

53. **Yan GX, Antzelevitch C.** Cellular basis for the normal t wave and the electrocardiographic manifestations of the long-QT syndrome. *Circulation* 98: 1928–1936, 1998.

54. **Zygmunt AC, Eddlestone GT, Thomas GP, Nesterenko VV, Antzelevitch C.** Larger late sodium conductance in M cells contrbutes to electrical heterogeneity in canine ventricle. *Am J Physiol Heart Circ Physiol* 281: H689–H697, 2001.

A Three-Dimensional Simulation Model of Cardiomyocyte Integrating Excitation-Contraction Coupling and Metabolism

Asuka Hatano,* Jun-ichi Okada, Takumi Washio, Toshiaki Hisada, and Seiryo Sugiura
Department of Frontier Science, The University of Tokyo, Kashiwa, Chiba, Japan

ABSTRACT   Recent studies have revealed that Ca^{2+} not only regulates the contraction of cardiomyocytes, but can also function as a signaling agent to stimulate ATP production by the mitochondria. However, the spatiotemporal resolution of current experimental techniques limits our investigative capacity to understand this phenomenon. Here, we created a detailed three-dimensional (3D) cardiomyocyte model to study the subcellular regulatory mechanisms of myocardial energetics. The 3D cardiomyocyte model was based on the finite-element method, with detailed subcellular structures reproduced, and it included all elementary processes involved in cardiomyocyte electrophysiology, contraction, and ATP metabolism localized to specific loci. The simulation results were found to be reproducible and consistent with experimental data regarding the spatiotemporal pattern of cytosolic, intrasarcoplasmic-reticulum, and mitochondrial changes in Ca^{2+}; as well as changes in metabolite levels. Detailed analysis suggested that although the observed large cytosolic Ca^{2+} gradient facilitated uptake by the mitochondrial Ca^{2+} uniporter to produce cyclic changes in mitochondrial Ca^{2+} near the Z-line region, the average mitochondrial Ca^{2+} changes slowly. We also confirmed the importance of the creatine phosphate shuttle in cardiac energy regulation. In summary, our 3D model provides a powerful tool for the study of cardiac function by overcoming some of the spatiotemporal limitations of current experimental approaches.

INTRODUCTION

In addition to their essential role in supplying energy to the heart, cardiac mitochondria have been observed to take up and release calcium (Ca^{2+}) in cardiomyocytes. However, although the Ca^{2+}-buffering capacity of the mitochondria is potentially significant, its contribution to excitation-contraction coupling through the regulation of cytosolic $[Ca^{2+}]$ has been proven to be negligible (1). Moreover, recent studies have identified further functional significance of mitochondrial Ca^{2+} flux, in that it provides a signal to activate the electron transport chain and ATP synthesis (2,3). Because the change in cytosolic Ca^{2+} concentration also serves as the signal for sarcomere contraction (the primary energy-consuming function of the myocyte), Ca^{2+} flux to the mitochondria may constitute a feed-forward regulatory mechanism for rapid fine-tuning of energy balance within the myocardium. Whether such a feed-forward mechanism is indeed stimulated by the beat-to-beat changes in the mitochondrial calcium concentration (fast Ca^{2+} uptake model) or by integrated changes in cytosolic Ca^{2+} concentration (slow Ca^{2+} uptake model) remains to be determined (4,5).

Prior studies have demonstrated, using Ca^{2+} indicators, that mitochondrial Ca^{2+} concentration changes from beat to beat (6,7); however, the high potential of signal interference from cytosolic Ca^{2+} cannot be excluded in these studies (5,8). On the other hand, where the cytoplasmic Ca^{2+} fluorescence was minimized, both slow (9–11) and fast (12,13) mitochondrial Ca^{2+} uptake has been reported.

Recent studies using genetically targeted mitochondrial Ca^{2+} probes reported the occurrence of fast Ca^{2+} uptake by the mitochondria, but with the slow decay of mitochondrial Ca^{2+} still apparent (14,15). Aside from the technical issues involved, research into the mode of mitochondrial Ca^{2+} uptake has demanded important mechanistic considerations. First, whereas the physiological Ca^{2+} transient peaks at 1–2 μmol/L under normal physiological conditions, the half-maximal effective concentration (EC_{50}) of the Ca^{2+} uniporter is reported to be much higher (16,17). Put simply, for the mitochondria to take up a significant amount of Ca^{2+} in this setting, the mitochondria must sense a transient increase in localized $[Ca^{2+}]$ (in the microdomain). To date, the existence of such a microenvironment has been suggested only indirectly or theoretically (13,18,19). Second, because mitochondrial Ca^{2+} cycling dissipates both membrane potential ($\Delta\Psi$) and ΔpH across the mitochondrial inner membrane, additional energy is required for their maintenance. In this sense, it is questionable whether the beat-to-beat adjustment of mitochondrial ATP synthesis to energy demand is cost-effective. Despite the recent advances in equipment and techniques, the current experimental approaches cannot provide us with sufficient resolution with regard to both space and time to resolve these unanswered questions.

Computer simulations are now used for a wide array of applications, facilitating the understanding of complex biochemical and physical processes, including those involved in the bioenergetics of cardiomyocytes (13,20–23). In addition to its potential as an alternative to exhaustive experiments, computer simulation also enables unobstructed observation of biological processes, as well as

accurate quantification of the processes occurring beyond the resolution limits of methods currently employed. However, the majority of simulated models constructed to date have primarily focused on the interactions of specific chemical species and elementary processes, with less attention afforded to the geometric aspects of organelle function or the physics underlying Ca^{2+} movement.

We previously developed a three-dimensional (3D) cardiomyocyte model based on the finite-element method, in which the Ca^{2+} wave and resultant contraction were reproducible and authentic (24). The study presented here significantly extends this line of research, enhancing the cardiomyocyte model by adding detailed subcellular structures, including the sarcolemma with t-tubule system, the SR (sarcoplasmic reticulum), the myofibril, and mitochondria. By solving the elementary processes in each organelle, diffusion of Ca^{2+} and energy metabolites, and deformation of the sarcomere induced by active contraction, this model is shown to successfully reproduce changes in cytosolic, intra-SR, and mitochondrial Ca^{2+} during contraction in various inotropic states observed by other experimental methods. Detailed analysis suggests that although the observed large cytosolic Ca^{2+} gradient facilitates uptake by the mitochondrial Ca^{2+} uniporter to produce beat-to-beat changes in mitochondrial Ca^{2+} concentration ($[Ca^{2+}]$) near the Z-line region, the average mitochondrial $[Ca^{2+}]$ changes slowly. We also confirmed the importance of the creatine phosphate shuttle in cardiac energy regulation. Our 3D model of cardiac excitation-contraction and metabolism provides a powerful tool for in-depth analysis of cardiac physiology and function, expanding the temporal and spatial limits of current experimental approaches.

MATERIALS AND METHODS

This model is an extension of our previous 3D cardiomyocyte model (24) to include metabolic processes as well as three features that distinguish it from our earlier model:

1. Detailed subcellular structures, including the sarcolemma with t-tubule system, SR, myofibril, and mitochondria, are reproduced in 3D space, arranged based on published reports.
2. The effect of specific reactions occurring within each functional component (metabolites or ions) able to diffuse across the cytosolic space in 3D, enabling observation of secondary effects at remote loci.
3. The contraction (cross-bridge) model was modified to include the dependence of force generation on metabolite level, sarcomere length, and shortening velocity. Force generation and the resultant deformation of finite elements were repeated to reproduce the true physiological contraction of the myocyte.

The 3D finite-element model of the myocyte

Fig. 1 A displays the structure of the 3D myocyte model. To reduce the computational cost, the segment was modeled to contain three myofibrils of one sarcomere length, together with the adjacent cell membrane and organelle. The rationale behind the modeling was that it reproduced longitudinal periodicity and axial symmetry of the myocyte. It was assumed that
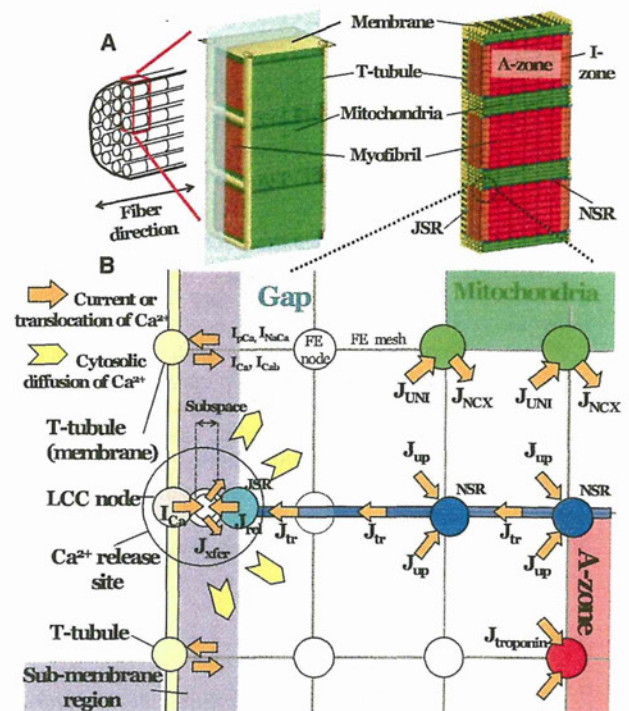
FIGURE 1 (A) 3D cardiomyocyte model consisting of three myofibrils of one sarcomere length, including adjacent cell membrane and organelles. The finite-element method was used for modeling. (B) Detailed illustration of the model near the t-tubule region including the pathways for Ca^{2+} regulation. J_x represents Ca^{2+} flux by either the uniporter (UNI) or the Na^+-Ca^{2+} exchanger (NCX), uptake by NSR (up), release from JSR (rel), transfer from NSR to JSR (tr), transfer from subspace to cytosol (xfer), or binding to troponin C (troponin). I_x represents the Ca^{2+} current from the LCC (Ca), sarcolemmal Ca^{2+} pump (pCa), Na^+-Ca^{2+} exchanger (NaCa), or background current (Cab). In this region, mesh sizes were made finer for more detailed analysis.

in a cylindrical myocyte containing 40 myofibrils, three radially arranged myofibrils occupied the space between the cell membrane and the center of the myocyte. At the final stage, further reductions were implemented so that only one-quarter of this model (halved in both length and width) was included for analysis. Such modeling of the small symmetrical segment due to the limited computational power prevented reproduction of local heterogeneity and the axial elements of the t-tubule structure. To overcome this, models were tested in which the t-tubule was partially deleted. Although local deletion of t-tubule induced slight delays in both the upstroke and decay of local Ca^{2+} transients, global behavior of the cell (Ca^{2+} transient, ADP, and SR $[Ca^{2+}]$) was not notably altered (Fig. S5 and Fig. S6 in the Supporting Material). In addition, L-type Ca^{2+} channels (LCCs) are not distributed in the axial elements of t-tubules (25); therefore, omission of the axial element from the model would not significantly affect Ca^{2+} handling. Accordingly, the original model illustrated in Fig. 1 was found to be sufficient and was used subsequently for all simulations. The 3D structure was modeled on a hexahedral solid finite-element model, consisting of 1861 nodes and 581 elements. The total numbers of degrees of freedom were 6164 for mechanical analyses and ~20,000 for physiological simulation. Subcellular components including the mitochondria, myofibril (A-zone, I-zone, and M-line), junctional and network SR (JSR and NSR, respectively), cell membrane, and t-tubules were located at the appropriate nodes to reproduce the anatomical structure and occupy the relative volume (1,26–28). Because the function of each subcellular component was

primarily based on the mathematical formulation proposed by Cortassa et al. (28), modeling of the excitation-contraction coupling of the guinea pig myocyte, the volume ratio of subcellular components (29), and ion channel distribution (30) was also adjusted based on the guinea pig cardiomyocyte. Each subcellular component could exchange ions and/or metabolites into the surrounding cytosol, and these molecules diffused freely through the cytosolic space.

Reaction-diffusion equations

Several investigations of Ca^{2+} dynamics utilizing 3D models have been reported (24). The study described here adopted these formulas for calculating the transport and exchange of metabolites and signaling molecules.

The multiple reaction-diffusion fields for Ca^{2+} and five substrates, including creatine (Cr), creatine phosphate (CP), inorganic phosphate (Pi), adenosine triphosphate (ATP), and adenosine diphosphate (ADP), were defined in the cytosolic space. The reaction-diffusion equations have the x axis in the longitudinal direction, with the z axis in the radial direction, as described below.

At a node where a functional component exists,

$$\frac{d[S]_i}{dt} = \nabla \cdot \left(D_i^s \nabla[S]_i\right) + f_i^s\left([Ca^{2+}]_i, [Cr]_i, [CP]_i, [Pi]_i, [ADP]_i, [ATP]_i\right). \tag{1}$$

Alternatively,

$$\frac{d[S]_i}{dt} = \nabla \cdot \left(D_i^s \nabla[S]_i\right). \tag{2}$$

S denotes one of the six substrates, i indicates the location (node), D_i^s is a diagonal matrix describing the diffusivity of substrate S, $[S]_i$ is the concentration of S at position i, and f_i^s is the function describing the reaction of substrate S.

Details of the reaction and diffusion processes near Ca^{2+} release sites are illustrated in Fig. 1 B. In this model, the LCC node, JSR node, subspace node, and cytosolic node are colocalized to the Ca^{2+} release site but possess their own Ca^{2+} concentrations for finite-element analysis. The current through the LCC (I_{Ca}) flows into the subspace and activates ryanodine receptors located on the JSR node. Ca^{2+} released from the JSR (J_{rel}) also flows into the subspace and thereafter moves to the cytosolic node to diffuse throughout the entire cytosol. Within the cytosolic space, Ca^{2+} is taken up by the Ca^{2+} uniporter of the mitochondrial node, bound to troponin C in the A-zone thin filament, and sequestered by SERCA2 on the NSR before eventually being transported back to the JSR. Further details outlining the model can be found in the Supporting Material. Similar calculations were performed at each node and for all the ions and metabolites, where pertinent.

Mitochondria and energy metabolism

To incorporate the high EC_{50} of the Ca^{2+} uniporter, we adopted the model proposed by Dash et al. (31). Because mitochondria are exposed to a large cytosolic Ca^{2+} gradient, it was hypothesized that a Ca^{2+} gradient may also exist in the mitochondrial matrix, enabling it to activate the tricarboxylic acid cycle to regionally upregulate NADH and ATP synthesis. To reproduce this process, the reaction-diffusion equation of Ca^{2+} inside the mitochondrial matrix was performed separately considering impermeability of the mitochondrial inner membrane. The exchanges of ions and metabolites between the cytosol and matrix via the inner membrane were mediated by channels and uniporters. The transport of ions and energy metabolites is diagrammed in Fig. S3.

ATP synthesized within the mitochondrial matrix is released into the intermembrane space via the adenine nucleotide translocator (ANT) and transferred to the site of ATP utilization via one of two major pathways, direct diffusion or creatine phosphate (CP) shuttle. In the CP shuttle, ATP is converted to easily diffusible CP by mitochondrial creatine kinase (Mit-CK) localized within the intermembrane space. After diffusion of CP to the site of energy utilization, CP is converted back to ATP through an inverse reaction. The myofibril is the major site of energy utilization, where the ATP regenerating system is localized at the M-line as M-line-bound CK (32). Because no regenerating system exists at the A-zone, I-zone, or Z-line, regenerated ATP diffuses to the A-zone from the M-line. The relative contribution of these two pathways to energy transfer is examined in this study.

Excitation-contraction coupling and myocyte shortening

To establish the link between cross-bridge kinetics and energy metabolism, we adopted the sarcomere model developed by Negroni et al. (33), with a modification made by Matsuoka et al. (34). This model was positioned at each point of the A-zone and generated force depending on the local Ca^{2+} and energy-metabolite concentrations. Using these force values, the mechanical equilibrium was calculated using the finite-element method, assuming hyperelasticity of the material (material properties are listed in Table S2 and Table S3, with validation in Fig. S7 and Fig. S8).

Study protocol

Simulations were performed at 0.5, 1, and 2 Hz. Data obtained at the 200th contraction (pseudo-steady state) were compared. The effect of β-adrenergic stimulation was examined by upregulation of both the LCC (to 125%) and SR Ca^{2+} pump (to 200%) based on prior reports (35,36). The transient response after an abrupt increase in pacing rate from 0.25 to 2 Hz was also examined. The parameters for slow (maximum rate of mitochondrial Ca^{2+} uniporter (V^{max}_{uni}) = 5.0×10^{-6} mM/ms, maximum rate of mitochondrial NCX (V^{max}_{NCX}) = 2.0×10^{-5} mM/ms) and fast (V^{max}_{uni} = 2.0×10^{-5} mM/ms, V^{max}_{NCX} = 8.0×10^{-5} mM/ms) mitochondrial Ca^{2+} handling were applied, and the steady states and transient responses were compared.

Computation

Computation was performed using an Intel Xeon CPU (3.2 GHz) and required 1000 s for a single cycle of 1 Hz contraction. All program codes were written in-house.

RESULTS

Ca^{2+} transients during contraction under steady-state conditions

Changes in $[Ca^{2+}]$, force, and [ADP] during free contractions at 1 Hz are illustrated as time-lapsed 3D images in Fig. 2, with other metabolites and mitochondrial Ca^{2+} illustrated in Fig. S10 and Movie S1. Ca^{2+} released from the JSR attains a high cytosolic concentration at both ends of the sarcomere but fades rapidly via uptake by the NSR as it diffuses toward the M-line (Fig. 2, left column). Force generation by the cross-bridges follows the $[Ca^{2+}]$ in the A-zone (Fig. 2, middle column). Accumulation of ADP also follows the course of force generation; however, spatial
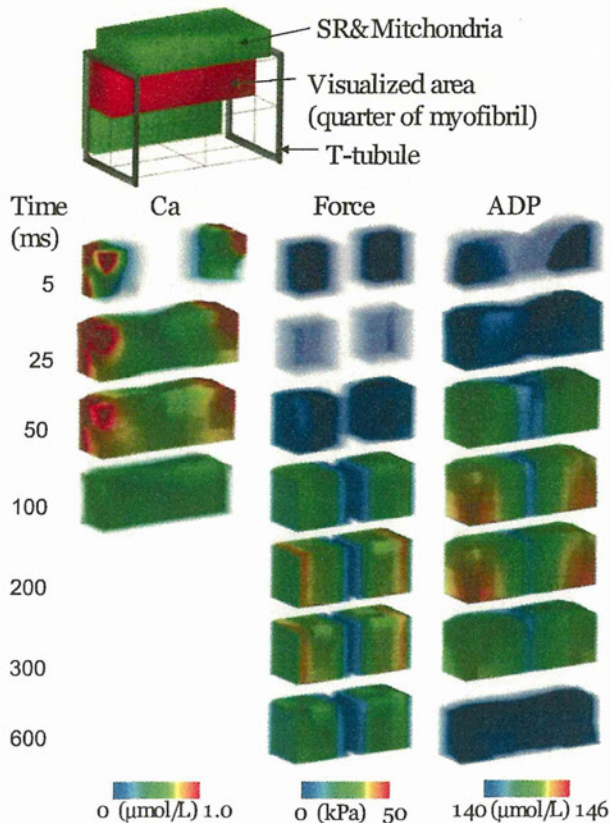
FIGURE 2 Time-lapse images displaying the spatial distribution of [Ca^{2+}], force, and [ADP]. Each panel represents one-quarter of one sarcomere. Numbers on the left indicate time (ms) after the onset of contraction.

FIGURE 3 Ca^{2+} transients at various loci are displayed in response to changes in length (*A*) or force (*E*) for unloaded (*left column*) and isometric (*right column*) contraction. Ca^{2+} transients were sampled at the SR and the subspace (*B* and *F*), the I-zone and A-zone (*C* and *G*), and the submembrane (*D*) and whole-cytosolic (averaged) regions (*H*). (*I*) Positions referred to in panels C–H. (*J*) Experimental data for the submembrane and bulk cytosolic Ca^{2+} transients (reproduced from Weber et al. (37) by copyright permission of the American Heart Association).

distributions were shifted toward the periphery (Z-line) due to the regeneration of ATP at the M-line and an enhanced ATP utilization rate (expressed as the rise in ADP level) caused by the high local [Ca^{2+}] (Fig. 2, *right column*). In this simulation of 1 Hz, sarcomere shortening was found to be 9%. Membrane potential and currents are shown in Fig. S9.

To further examine the spatiotemporal distribution of Ca^{2+} displayed in Fig. 2, local Ca^{2+} signals were sampled at various points in the cytosolic space and SR under both shortening and isometric conditions and plotted with the time course of length and force for each contraction mode (Fig. 3). The beginning of both shortening (Fig. 3 *A*) and isometric (Fig. 3 *E*) contraction was associated with an immediate rise in Ca^{2+} within the subspace (peaking at ~100 μM). This rise coincided with a reduction in SR Ca^{2+} (Fig. 3, *B* and *F*). Ca^{2+} transients in the submembranous space (~20 nm from the t-tubule (Fig. 3 *I*)) were plotted with cytosolic [Ca^{2+}] (Fig. 3, *C* and *G*). Similar to the subspace, submembranous Ca^{2+} transients peaked rapidly, although they only reached ~4 μM, comparable to previous experimental findings (Fig. 3 *J* (37)). Cytosolic [Ca^{2+}] was averaged over the entire model except mitochondrial space,
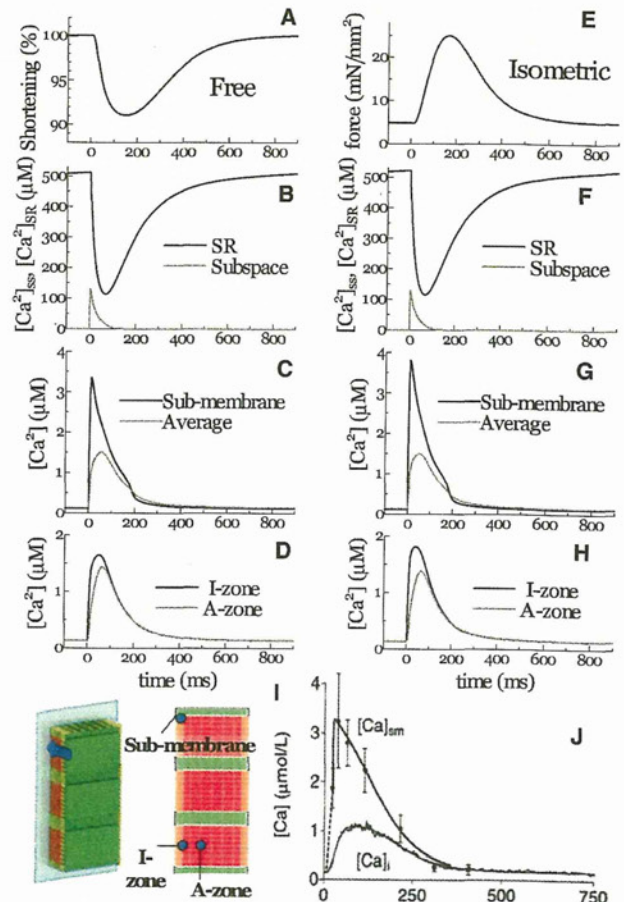
assuming that the experimentally recorded Ca^{2+} signal reflects the fluorescence averaged over the sarcomere. The averaged cytosolic Ca^{2+} transients determined by the current simulation were in agreement with published experimental results (Fig. 3 *J* (37)), supporting the validity of this model. Within the cytosolic space, data were recorded along the center of the sarcomere at two points, 0.1 μm (I-zone) and 0.7 μm (A-zone), respectively, from the Z-line (Fig. 3, *D* and *H*). In the I-zone, the Ca^{2+} transient peak was lower (~1.6 μM) and delayed (~40 ms under free contractions and ~50 ms under isometric conditions) after depolarization. Ca^{2+} peaks at the A-zone were further reduced and delayed (~65 ms) compared to the I-zone under both isometric and free conditions.

Investigating the issue of a fast- or slow-uptake model for mitochondrial Ca^{2+} handling, we compared the simulation

results based on the fast and slow parameter sets with experimental observations (13). For this purpose, mitochondrial and cytosolic Ca^{2+} transients were compared before and after positive inotropic intervention (Fig. 4, C and D (13)). Positive inotropy was stimulated by upregulation of both the LCC and the SR Ca^{2+} pump. Inotropic intervention increased the peak amplitude of the cytosolic Ca^{2+} transient and accelerated its rapid decay (Fig. 4 A, *dashed line*) when compared to control (*solid line*), as reported in the experiment (Fig. 4 C (13)). Global mitochondrial Ca^{2+} transients averaged over the entire mitochondrial space increased in amplitude and baseline levels (compare Fig. 4 B, *solid* and *dashed lines*) in both fast (*red lines*) and slow (*black lines*) models. The fast model produced greater magnitudes of mitochondrial $[Ca^{2+}]$ compared to the slow model, thus reproducing the experimental results (Fig. 4, C and D). However, observing the local mitochondrial Ca^{2+} transient near the Ca^{2+} release site under slow model conditions, its amplitude was found to be even larger than under fast model conditions (*blue lines*). Please note that its steep upstroke also resembles the experimental observation.

Transient responses

The responses of $[Ca^{2+}]_{mito}$ and [NADH] to abrupt changes in pacing rate were compared between the simulation presented here (Fig. 5, A and B) and the experimental results reported by Brandes and Bers in rat trabeculae (Fig. 5, C and D (38)). Following the experimental protocol of Brandes and Bers (38), the pacing frequency was abruptly
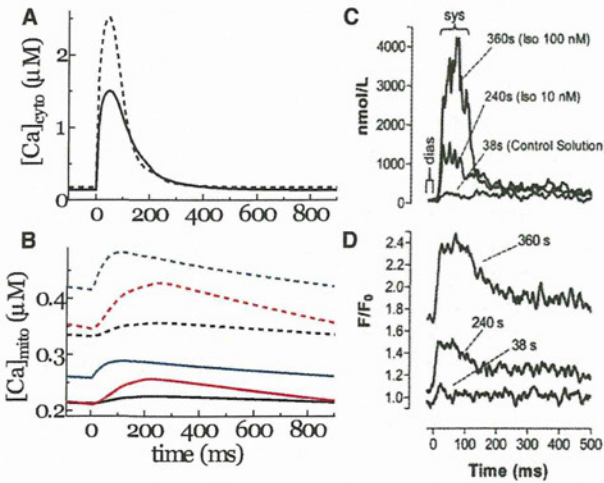
FIGURE 5 Simulated transient response of $[Ca]_{mito}$ (A) and [NADH] (B) are compared to prior experimental observations of NADH (C) and mitochondrial Ca^{2+} (D) after an increase in stimulation frequency from 0.25 to 2 Hz in rat cardiac trabeculae (reproduced from Brandes and Bers (38) by copyright permission of the Biophysical Society). Under the simulation model, two sets of parameters, fast (*red line*) and slow (*black line*), are used.

increased from 0.25 Hz to 2 Hz, then relaxed back to 0.25 Hz. Both the fast and slow parameter sets were applied under these conditions, and the results were compared. When subjected to the fast parameters, the change in pacing rate caused a significant increase in mitochondrial Ca^{2+} transient amplitude (Fig. 5 A, *red line*). In contrast to the experimental results, the simulation failed to reveal either undershooting or overshooting of NADH (Fig. 5 B (*red line*) and D (38)). In contrast, under the slow parameters, the NADH response displayed both undershooting and overshooting (Fig. 5 B, *black line*), correlating with the rise of mitochondrial Ca^{2+} (Fig. 5 A, *black line*), consistent with the experimental results. Taken together, the mitochondrial Ca^{2+} transient produced by our simulation model is consistent with experimental findings only under slow Ca^{2+} handling parameters.

Energy metabolism

Temporal changes in the concentrations of energy metabolites at various loci within the sarcomere were plotted with $[Ca^{2+}]$ at three different pacing rates (Fig. 6 and Fig. S10). The concentration of Ca^{2+} was found to decrease rapidly after peaking near the Z-line with a progressive delay in its peak timing when approaching the M-line (Fig. 6, *top row*). ADP accumulation was found to occur in the Z-line half of the sarcomere, but displayed no delay in its timing (Fig. 6, *second row*). The concentration of creatine increased gradually but homogeneously along the fiber direction due to its high diffusivity (Fig. 6, *third row*). These trends were common to all three pacing conditions tested. In contrast, the response of ANT activity (V_{ANT}) in the mitochondria displayed a unique dependence on the pacing rate (Fig. 6, *bottom row*). At low pacing (0.5 Hz), V_{ANT} peaked at ~100 ms near the Z-line (early peak), with

FIGURE 4 (A and B) Cytosolic (A) and mitochondrial (B) Ca^{2+} transients subjected to control (*solid line*) or positive inotropic (*dashed line*) conditions. Averaged mitochondrial Ca^{2+} transients under slow (*black line*) and fast (*red line*) parameters for mitochondrial Ca^{2+} handling, and local mitochondrial Ca^{2+} transient under slow parameters are compared in B. (C and D) Prior experimental data for cytosolic (C) and mitochondrial (D) Ca^{2+} transients from Maack et al. (13) are provided for comparison (by copyright permission of the American Heart Association).
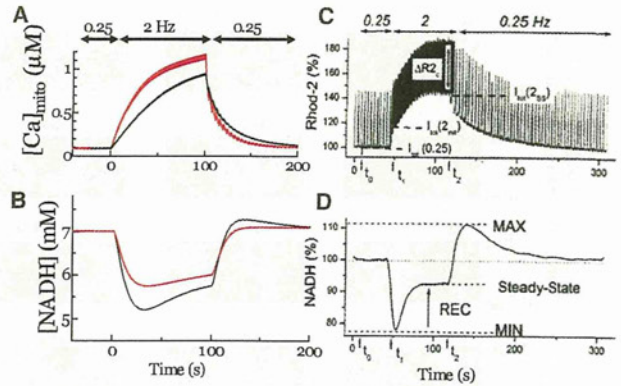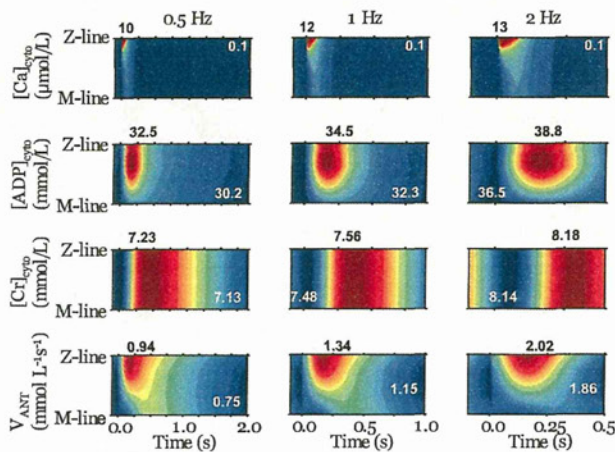
FIGURE 6 Spatiotemporal patterns of (*top to bottom*) $[Ca^{2+}]_{cyto}$, $[ADP]_{cyto}$, $[Cr]_{cyto}$, and ANT exchange velocity. Results for loading of 0.5 Hz (*left column*), 1 Hz (regarded as control) (*middle column*), and 2 Hz (*right column*) are compared. Each panel presents data from half of one sarcomere, with the Z-line at the top and the M-line at the bottom, after each stimulus. Maximum values (*dark red*) are given by black numbers above the panels, and minimum values (*dark blue*) by white letters in the panels.

a less prominent peak also apparent (*yellow green*) at ~400 ms near the M-line (late peak), which coincided with the peak of Cr. The late peak became diminished with increased pacing, and at 2 Hz was no longer evident.

The total amount of ATP synthesis occurring within the sarcomere was compared with the amount converted to CP when subjected to 0.5, 1, or 2 Hz of pacing. The fraction of energy supplied by the CP shuttle system was calculated to be 48.8% (76.1 of 155 μmol L^{-1} s^{-1}) at 0.5 Hz, 47.4% (114 of 241 μmol L^{-1} s^{-1}) at 1 Hz, and 46.5% (183 of 393 μmol L^{-1} s^{-1}) at 2 Hz.

DISCUSSION

An integrated model of cardiomyocyte function

This study employed a 3D cardiomyocyte model in which the electrical, energetic, and mechanical dynamics were integrated with detailed ultrastructures. There have been several previous attempts to develop computational models capable of coupling electrophysiology and Ca^{2+} handling with mitochondrial energetics (28,34); however, because the majority of these models are lumped-parameter models, assuming microcompartments of reaction pools to avoid the computationally challenging partial differential equations, these models only provide us with spatially averaged behavior of ions and metabolites. More intricate models that account for the spatiotemporal pattern of subcellular activities have been developed, but these models have focused only on the transfer of energy metabolites (20,39). To our knowledge, this is the first 3D model to define

myocardial energetics coupled with both electrophysiology and Ca^{2+} handling, and to be capable of reproducing the reaction-diffusion phenomena involved in cardiac energy production and utilization. The results obtained using this model go a long way toward explaining some of the controversies currently debated in the field of myocardial energy dynamics, as this model is not subject to the spatiotemporal resolution limitations imposed by current experimental techniques.

Comparison with previous experimental studies

The current simulation model successfully reproduced fundamental contractile characteristics of the cardiac sarcomere. Not only was the average cytosolic [Ca^{2+}] (~1 μM) amplitude and [Ca]$_{SR}$ profile typical of a cardiac sarcomere (Figs. 3, *B* and *F*, and 4, *A* and *C*), but the subcellular distributions and temporal changes of Ca^{2+} were also consistent with previous investigations. For example, Weber et al. (37) estimated the submembrane [Ca^{2+}] ([Ca^{2+}]$_{sm}$), sensed by the Na-Ca exchanger (NCX) by determining the NCX tail current and bulk [Ca^{2+}] ([Ca^{2+}]$_b$) transient. They revealed that the [Ca^{2+}]$_{sm}$ reaches its peak in <32 ms of the action-potential upstroke, and to a level higher than bulk [Ca^{2+}] (Fig. 3 *I*). Consistent with this observation, submembrane [Ca^{2+}] in our simulation was found to peak at 10 ms (~4 μM) (Fig. 3, *C* and *G*). Observing the subspace [Ca^{2+}], no experimental data have been reported to date, although several numerical estimates using detailed diad geometry (40,41) yield values similar to those of the simulation presented here (Fig. 3, *B* and *F*). As for the effect of contraction mode, the peaks of local Ca^{2+} transients under isometric conditions were found to be higher in the submembrane region and I-zone, but reduced in the A-zone compared to the Ca^{2+} transients under free contraction (compare Fig. 3, *C* and *G*, and Fig. 3, *D* and *H*). Furthermore, the time to peak in the I-zone was faster by 10 ms. These differences in Ca^{2+} dynamics observed under different loading conditions are due to the increase in diffusion distance caused by widening of the myocyte; however, we are unaware of any comparable experimental data. On the other hand, the global Ca^{2+} transient did not differ between the isometric and free-contraction modes (compare Fig. 3, *C* and *G*). This finding supports a previous study by White et al. indicating that altering length had no effect on the global Ca^{2+} transient in guinea pig myocytes (42). In contrast, Yasuda et al. reported a significant increase in Ca^{2+} transient peak during shortening contraction in rat ventricular myocytes (43). The cause of this discrepancy remains to be confirmed, but the strain dependence of affinity of Ca^{2+} for troponin C, which we did not incorporate into this model, could be a factor.

Some studies using ^{31}P NMR (44,45) have identified cyclic changes in high-energy phosphate levels (~10%) during the cardiac cycle. However, other studies have found

that cyclical changes are undetectable, or estimated to be only 1.6%, even assuming instantaneous ATP hydrolysis with no resynthesis (46,47). The reason for this discrepancy is not clear, but as discussed by Illing et al. (44), cyclic changes are mainly found with a high heart rate under crystalline perfusion (inadequate substrate supply) and in vivo large animal studies (low heart rate and blood perfusion) were unable to detect ATP cycling. Our model assumed an adequate substrate supply and reproduced cyclic changes in these metabolites (Fig. 6), but the relative amplitude was small (<1%). Consistent with these results, a simulation study that took into account the effect of high subsarcolemmal Ca^{2+} concentration on the regulation of metabolite concentrations reported even smaller fluctuations (48).

Mitochondrial response

In response to experimentally induced changes in the pacing rate, $[Ca]_{mito}$ is reported to increase or decrease gradually, whereas NADH levels are reported to undershoot and overshoot at the transitions (Fig. 5, C and D) (38). Our simulation reproduced these responses in $[Ca^{2+}]_{mito}$ and NADH, paralleling the experimental findings over time; however, these effects were only produced under the slow parameters for mitochondrial Ca^{2+} handling (Fig. 5, A and B). Despite these promising comparative results, the large beat-to-beat oscillations in $[Ca^{2+}]_{mito}$ were not observed in our simulation, nor in the simulation study of Cortassa et al. (28). For the large beat-to-beat oscillations in $[Ca]_{mito}$ to occur, the mitochondrial Ca^{2+} uniporter must encounter high local $[Ca^{2+}]_{cyto}$ due to its high EC_{50}. In addition, a high velocity of mitochondrial Ca transport is required. Because our simulation is comprised of a high submembrane $[Ca^{2+}]_{cyto}$, the fast parameters, i.e., high V^{uni}_{max} and high V^{NCX}_{max}, reproduced the large beat-to-beat $[Ca^{2+}]_{mito}$ oscillations (Fig. 4 B, solid lines); however, the under- and overshooting of NADH disappeared under fast parameters (Fig. 5 B, red line). The disparities between our model and prior experimental reports of beat-to-beat $[Ca^{2+}]_{mito}$ oscillations and NADH levels may be explained by the following two possibilities. 1), The experimentally determined fluorescent Ca^{2+} signal may come preferentially from near the Z-line region, where a large transient with steep upstroke can be obtained in our simulation under slow parameters (Fig. 4 B, blue lines). 2), The disparity may be due to potential errors in modeling the NCX, originating from the controversies of its stoichiometry (49) and K_m dependency on matrix pH (50).

The predicted reductions in cytosolic Ca^{2+} transients due to mitochondrial uptake at 1 Hz were ~2% and 7% under slow and fast mitochondrial Ca^{2+} handling parameters, respectively. Most experimental estimates suggest that this fraction is <~2% (1), supporting the slow model, but one study reported values as high as ~36% (13), which were estimated from large beat-to-beat $[Ca^{2+}]_{mito}$ oscillations.

The above discussion may be applied to reconcile such discrepant findings, and in fact, the latter study also suggested that the close proximity of the mitochondria to the Z-line region is the key to realizing a fast response. The authors of that study also performed numerical simulations to reproduce large cyclic changes in $[Ca^{2+}]_{mito}$ by referring to the $[Ca^{2+}]$ in subspace, but metabolic processes were not included in their model.

Finally, it is notable that $[Ca^{2+}]_{mito}$ is not solely governed by the mitochondrial Ca^{2+} uniporter sensing transient high $[Ca^{2+}]_{cyto}$ induced by SR Ca^{2+} release. During the resting phase, Ca^{2+} extrusion by NCX in t-tubules lowers $[Ca^{2+}]_{cyto}$ to near the Z-line region to facilitate the release flux of Ca^{2+} by mitochondrial NCX. In addition, because the actions of the mitochondrial uniporter and NCX are driven by the inner membrane potential, the energetic state also affects mitochondrial Ca^{2+} cycling.

Functional significance of the CP shuttle

Comparison of the findings of spatiotemporal distribution of energy metabolites under different loading conditions suggests the functional significance of CP shuttling. At 0.5 Hz, ANT activity was found to peak at ~100 ms at loci near the Z-line (Fig. 6, bottom row, left), which coincides with the peak of ADP (Fig. 6, second row, left). Because [ADP] preferentially increases in this region, it is natural to consider that this early peak in ANT activity is induced by the ADP diffusing into the mitochondria. However, we found that the region of high [ADP] is shifted to the I-band rather than to the A-band, where ATP consumption is high (Fig. 6, second row, and Fig. 2). This shift in ADP distribution, caused by M-line-bound CK, may be beneficial for force generation, by avoiding the accumulation of ADP around cross-bridges at the A-band. It is interesting that we identified another less prominent peak in V_{ANT} at 400 ms, coinciding with the Cr peak. It appears that this late peak of V_{ANT} may extend toward the Z-line, delaying the decay of ANT activity near the Z-line. Although ANT is not directly activated by Cr, such a spatiotemporal coincidence suggests that the Cr-CP system is capable of modulating mitochondrial activity without raising the ADP level at the A-band.

As the pacing rate was increased, the late V_{ANT} peak became less prominent, and at 2Hz, it had ceased to exist, with only the early peak at ~100 ms (Fig. 6, bottom row, right), despite Cr maintaining its delayed peak, as observed under lower loading conditions. Further analysis revealed that the concentration of Cr, even at its nadir, is much greater than the peak value observed under control conditions (Fig. 6, third row). We hypothesize that this is likely due to the limited capacity of the mitochondria to maintain the energy balance in response to the excessive amount of ADP produced. This would subsequently cause [Cr] to remain elevated throughout the relaxation phase. Put simply,